The Journal of Chemical Physics

Potential energy and dipole moment surfaces of the triplet states of the $O_2(X^3\Sigma_g^-)$ – $O_2(X^3\Sigma_g^-, a^1\Delta_g, b^1\Sigma_g^+)$ complex

Cite as: J. Chem. Phys. **147**, 084306 (2017); https://doi.org/10.1063/1.4990661
Submitted: 16 June 2017 . Accepted: 27 July 2017 . Published Online: 31 August 2017

Tijs Karman, Ad van der Avoird, and Gerrit C. Groenenboom

Potential energy and dipole moment surfaces of the triplet states of the $O_2(X^3\Sigma_g^-) - O_2(X^3\Sigma_g^-, a^1\Delta_g, b^1\Sigma_g^+)$ complex

Tijs Karman, Ad van der Avoird, and Gerrit C. Groenenboom[a)]
Theoretical Chemistry, Institute for Molecules and Materials, Radboud University, Heyendaalseweg 135, 6525 AJ Nijmegen, The Netherlands

(Received 16 June 2017; accepted 27 July 2017; published online 31 August 2017)

We compute four-dimensional diabatic potential energy surfaces and transition dipole moment surfaces of O_2–O_2, relevant for the theoretical description of collision-induced absorption in the forbidden $X^3\Sigma_g^- \to a^1\Delta_g$ and $X^3\Sigma_g^- \to b^1\Sigma_g^+$ bands at 7883 cm^{-1} and 13 122 cm^{-1}, respectively. We compute potentials at the multi-reference configuration interaction (MRCI) level and dipole surfaces at the MRCI and complete active space self-consistent field (CASSCF) levels of theory. Potentials and dipole surfaces are transformed to a diabatic basis using a recent multiple-property-based diabatization algorithm. We discuss the angular expansion of these surfaces, derive the symmetry constraints on the expansion coefficients, and present working equations for determining the expansion coefficients by numerical integration over the angles. We also present an interpolation scheme with exponential extrapolation to both short and large separations, which is used for representing the O_2–O_2 distance dependence of the angular expansion coefficients. For the triplet ground state of the complex, the potential energy surface is in reasonable agreement with previous calculations, whereas global excited state potentials are reported here for the first time. The transition dipole moment surfaces are strongly dependent on the level of theory at which they are calculated, as is also shown here by benchmark calculations at high symmetry geometries. Therefore, *ab initio* calculations of the collision-induced absorption spectra cannot become quantitatively predictive unless more accurate transition dipole surfaces can be computed. This is left as an open question for method development in electronic structure theory. The calculated potential energy and transition dipole moment surfaces are employed in quantum dynamical calculations of collision-induced absorption spectra reported in Paper II [T. Karman *et al.*, J. Chem. Phys. **147**, 084307 (2017)]. *Published by AIP Publishing.* [http://dx.doi.org/10.1063/1.4990661]

I. INTRODUCTION

With an abundance of 21%, molecular oxygen is an important constituent of Earth's atmosphere. The $X^3\Sigma_g^-$ ground state of molecular oxygen corresponds to a $2p\sigma_g^2 2p\pi_u^4 2p\pi_g^{*2}$ configuration. There exist two low-lying excited states of $a^1\Delta_g$ and $b^1\Sigma_g^+$ symmetry corresponding to the same electronic configuration at 7883 cm^{-1} and 13 122 cm^{-1} above the ground state, respectively. Emission due to transitions from these states to the ground state can be observed in the atmosphere.[1] Absorption due to the $X^3\Sigma_g^- \to b^1\Sigma_g^+$ transition is used to calibrate satellite instruments and hence is important for remote sensing applications.[2] Excited states corresponding to different electronic configurations are also observed in the atmosphere. Atmospheric oxygen shows strong absorption bands in, for example, the Schumann-Runge continuum ($X^3\Sigma_g^- \to B^3\Sigma_u^-$) and Herzberg bands ($X^3\Sigma_g^- \to A^3\Sigma_u^+$, $X^3\Sigma_g^- \to A'^3\Delta_u$, and $X^3\Sigma_g^- \to c^1\Sigma_u^-$). The Herzberg transitions are electric-dipole forbidden but gain intensity due to spin-orbit and orbit-rotation coupling.[3]

Electric dipole transitions from the $X^3\Sigma_g^-$ ground state to the $a^1\Delta_g$ and $b^1\Sigma_g^+$ states are forbidden by multiple selection rules, e.g., the electronic spin quantum number changes, $S = 1 \nleftrightarrow 0$, the parity is conserved, $g \nleftrightarrow g$, and $\Delta\Lambda = 2$ for the transition to the $a^1\Delta_g$ state. Spin-orbit coupling between the $X^3\Sigma_g^-$ and $b^1\Sigma_g^+$ states breaks spin symmetry and allows for magnetic dipole $X^3\Sigma_g^- \to b^1\Sigma_g^+$ transitions[4,5] and electric quadrupole $X^3\Sigma_g^- \to a^1\Delta_g$ transitions.[6] Magnetic dipole coupling between the $X^3\Sigma_g^-$ and $a^1\Delta_g$ states involves spin-orbit coupling to intermediate excited states of $^1\Pi_g$ and $^3\Pi_g$ symmetry, and hence magnetic dipole transitions between these states are weaker.[7] Electric dipole transitions are allowed only after breaking both spin and inversion symmetry; thus, the dominant mechanism for this should be the collision with a paramagnetic species. In the atmosphere, the most abundant paramagnetic species is molecular oxygen itself. Due to the weak magnetic dipole strength for the $X^3\Sigma_g^- \to a^1\Delta_g$ transition, O_2–O_2 collision-induced absorption should contribute significantly to the band intensity under atmospheric conditions. Even for the $X^3\Sigma_g^- \to b^1\Sigma_g^+$ transition, where the magnetic dipole lines are relatively stronger, O_2–O_2 collision-induced absorption is important to achieve high accuracy in satellite calibration.[8]

In this paper, we investigate the potential energy and transition dipole moment surfaces of the O_2–O_2 complex, which are relevant to the theoretical description of collision-induced

a)Electronic mail: gerritg@theochem.ru.nl

absorption in the $X^3\Sigma_g^- \rightarrow a^1\Delta_g$ and $X^3\Sigma_g^- \rightarrow b^1\Sigma_g^+$ bands. The required dipole moment surfaces are the transition dipole moments from the triplet $O_2(X^3\Sigma_g^-)$+$O_2(X^3\Sigma_g^-)$ ground state to the four states correlating to $O_2(X^3\Sigma_g^-) + O_2(a^1\Delta_g)$ and to the two states correlating to $O_2(X^3\Sigma_g^-) + O_2(b^1\Sigma_g^+)$. The required adiabatic potential energy surfaces are those corresponding to the lowest seven triplet states of the O_2–O_2 complex. We also transform to a diabatic representation, using a recently developed multiple-property-based method.[9] This is necessary as the asymptotically degenerate excited electronic states of the complex are close in energy for all geometries, making non-adiabatic interactions non-negligible. The vibrational dependence of the potential energy and transition dipole moment surfaces is neglected in this first *ab initio* study of collision-induced absorption in this system but will be explored in a subsequent publication.[10]

Several global potentials for the singlet, triplet, and quintet spin states of the dimer correlating to the $O_2(X^3\Sigma_g^-) - O_2(X^3\Sigma_g^-)$ ground state exist in the literature. The Nijmegen potential is the first global potential consisting of *ab initio* first-order exchange and electrostatics with empirical dispersion contributions.[11–13] The Perugia potential was obtained by an inversion procedure on scattering cross sections from molecular beam experiments.[14,15] The Madrid-Cuernavaca potential is the most recent and most accurate potential. It consists of a quintet potential calculated with the accurate coupled-cluster method, combined with exchange splittings calculated using second-order complete active space perturbation theory (CASPT2) and multi-reference configuration interaction (MRCI).[16–19] For states of the O_2–O_2 dimer correlating to the monomers in electronically excited $a^1\Delta_g$ or $b^1\Sigma_g^+$-states, no global potential energy surfaces exist. *Ab initio* calculations for a limited number of orientations with high point-group symmetry have been performed,[20,21] which have been used in model calculations for the quenching of O_2 molecules in the $a^1\Delta_g$ state[20] and highly vibrationally excited ($v > 25$) $X^3\Sigma_g^-$ O_2 molecules.[22] For the present purpose of calculating collision-induced absorption spectra, global potentials and dipole surfaces are required, and calculations for only highly symmetric orientations of the molecules are not sufficient.

In Ref. 18, multi-reference methods have been compared systematically to more accurate single-reference coupled cluster [CCSD(T)] calculations for the high-spin quintet state correlating to $O_2(X^3\Sigma_g^-) - O_2(X^3\Sigma_g^-)$. The tested multi-reference methods were MRCI, CASPT2, and averaged coupled-pair functional (ACPF). It is suggested that we regard the MRCI and CASPT2 results as upper and lower limits to the potential energy, respectively, and it is made plausible that the CASPT2 results should be considered more reliable.[18] Nevertheless, we use the MRCI method in this work since this allows for straightforward calculation of transition properties. The calculation of transition moments is required for the transition dipole moment surface as well as for the multiple-property-based diabatization.

In the present work, we perform similar benchmark calculations at highly symmetric geometries, for both the interaction energy as well as the transition dipole moment. These calculations show that the interaction energy converges reasonably smoothly, albeit slowly, with the active space and basis set such that accurate results may be expected from affordable MRCI calculations. For the transition dipole moment, the situation is markedly different as the computed property depends strongly on the level of theory used. It may come as a surprise that we cannot obtain converged transition dipole moments, but this is in agreement with the work of Zagidullin *et al.*,[23] who studied the interaction-induced luminescence of $O_2(a^1\Delta_g)$ using a statistical model. In that work, it is shown that the interaction-induced dipole changes dramatically between complete active space self-consistent field (CASSCF) and MRCI levels of theory even with a large full-valence active space. Interaction-induced luminescence and collision-induced absorption are related by detailed balance. The authors of Ref. 23 consider a different transition, namely, between the $O_2(a^1\Delta_g) - O_2(a^1\Delta_g)$ excited state and the singlet ground state of the dimer. However, the mechanism for this transition is very similar, i.e., it is also allowed by the exchange interaction between two O_2 monomers, which breaks the spin symmetry. We also note that in Refs. 7, 24, and 25 and references therein, large electric dipole moments are obtained for spin-forbidden intersystem crossings in small organic molecules, induced by the exchange interaction with molecular oxygen.

This paper is organized as follows. Section II describes the theory. We give a brief summary of the multiple-property-based diabatization method of Ref. 9 and show how to include spin-orbit coupling in the diabatic model. The angular expansion of diabatic potential energy and transition dipole moment surfaces is discussed, and we derive restrictions on the expansions from inversion, time reversal, and permutation symmetry. We present formulas for determining the expansion coefficients by numerical integration, e.g., using Gauss-Legendre and Gauss-Chebyshev quadratures. Section III discusses the results of benchmark calculations, performed in order to estimate the accuracy of the calculation of both the potential energy and the transition dipole moments. Details of the calculations performed to obtain global potentials and dipole moment surfaces are given in Sec. IV. Section V describes an interpolation method with exponential extrapolation, which is used to represent the O_2–O_2 distance dependence of the angular expansion coefficients. The resulting four-dimensional potential energy and transition dipole moment surfaces are discussed in Sec. VI and conclusions are given in Sec. VII.

II. THEORY

A. Monomer electronic states and the diabatic model

In this section, we revisit a recently reported multiple-property-based diabatization scheme.[9] This scheme fits a unitary transformation between two representations, the adiabatic representation and the quasi-diabatic representation, given a set of molecular properties, evaluated in both bases. Properties in the adiabatic representation are routinely calculable in many electronic structure codes. Properties in the diabatic representation are determined in a system-specific model, which is discussed in this section. We extend the diabatic model in Ref. 9 to include spin-orbit coupling. This section also

provides the definition of the coordinate system and a discussion of the electronic states of interest.

We consider the low-lying excited states of the O_2 molecule discussed in the Introduction, i.e., the $X^3\Sigma_g^-$ ground state, the $a^1\Delta_g$ excited state at 7883 cm^{-1} above the ground state, and the $b^1\Sigma_g^+$ excited state at 13 122 cm^{-1}. The internuclear axis of molecule A with respect to an arbitrary space-fixed coordinate system is given by the vector $\boldsymbol{r}_A$. We will interchangeably denote the direction of this axis by the vector $\boldsymbol{r}_A$, by its polar angles, θ_A, ϕ_A, or by the zyz Euler angles $(\phi_A, \theta_A, 0)$. We calculate the monomer electronic wavefunctions for these states by solving the time-independent Schrödinger equation for a single O_2 molecule aligned with the z-axis, i.e., $\theta_A = \phi_A = 0$, and its center of mass as the origin of this monomer-fixed reference frame

$$\hat{\mathcal{H}}_{A,0}|\psi_A(0,0,0)\rangle = \epsilon_{\psi_A}|\psi_A(0,0,0)\rangle, \tag{1}$$

where ψ_A is any one of $X^3\Sigma_g^-$, $a^1\Delta_g$ or $b^1\Sigma_g^+$. The $a^1\Delta_g$ state is doubly degenerate with real-valued Cartesian components $a^1\Delta_{xy}$ and $a^1\Delta_{x^2-y^2}$ or the complex $\hat{L}_z$-adapted components

$$|a^1\Delta_{\pm 2}\rangle = \frac{1}{\sqrt{2}}\left(|a^1\Delta_{x^2-y^2}\rangle \pm i|a^1\Delta_{xy}\rangle\right), \tag{2}$$

which are eigenstates of $\hat{L}_z$ at eigenvalues $\Lambda = \pm 2$, respectively. The electronic Hamiltonian for an O_2 molecule along the vector $\boldsymbol{r}_A$ is found by rotating the electron coordinates as

$$\hat{\mathcal{H}}_A(\boldsymbol{r}_A) = \hat{\mathcal{R}}(\boldsymbol{r}_A)\hat{\mathcal{H}}_{A,0}\hat{\mathcal{R}}^\dagger(\boldsymbol{r}_A), \tag{3}$$

and for the eigenfunctions of this Hamiltonian, we find

$$\begin{aligned}\hat{\mathcal{H}}_A(\boldsymbol{r}_A)|\psi_A(\phi_A,\theta_A,0)\rangle &= \epsilon_{\psi_A}|\psi_A(\phi_A,\theta_A,0)\rangle,\\ |\psi_A(\phi_A,\theta_A,0)\rangle &= \hat{\mathcal{R}}(\phi_A,\theta_A,0)|\psi_A(0,0,0)\rangle,\\ \hat{\mathcal{R}}(\phi,\theta,\chi) &= \exp(-i\phi\hat{L}_z)\exp(-i\theta\hat{L}_y)\exp(-i\chi\hat{L}_z)\end{aligned} \tag{4}$$

with $\hat{\boldsymbol{L}}$ as the electronic orbital angular momentum operator. The orbital angular momentum $\hat{\boldsymbol{L}}$ generates rotations of the spatial part of the electronic wavefunctions and does not act on an electron spin. The advantage of this will become apparent below.

The geometry of a dimer consisting of two O_2 monomers, labeled A and B, is defined by three vectors $\boldsymbol{r}_A$, $\boldsymbol{r}_B$, and $\boldsymbol{R}$ with respect to some arbitrary space-fixed reference frame. The electronic Hamiltonian depends parametrically on these coordinates and is denoted as $\hat{\mathcal{H}}(\boldsymbol{r}_A, \boldsymbol{r}_B, \boldsymbol{R})$. The first two vectors define the length and direction of the molecular axes, as discussed above, whereas $\boldsymbol{R}$ points from the center of mass of molecule A to molecule B, i.e., with the dimer center of mass as the origin, monomer A is centered at $-\boldsymbol{R}/2$, and monomer B is centered at $\boldsymbol{R}/2$. For vanishing interaction, e.g., $R \to \infty$, the eigenstates are thus given as products of rotated and translated monomer states,

$$\begin{aligned}|\psi_A\psi_B\rangle^{(\boldsymbol{r}_A,\boldsymbol{r}_B,\boldsymbol{R})} &= \left[\hat{\mathcal{T}}(-\boldsymbol{R}/2)\hat{\mathcal{R}}(\boldsymbol{r}_A)|\psi_A(0,0,0)\rangle\right]\\ &\quad\otimes\left[\hat{\mathcal{T}}(\boldsymbol{R}/2)\hat{\mathcal{R}}(\boldsymbol{r}_B)|\psi_B(0,0,0)\rangle\right],\\ \hat{\mathcal{T}}(\boldsymbol{R}) &= \exp(-i\boldsymbol{R}\cdot\hat{\boldsymbol{P}}),\end{aligned} \tag{5}$$

with $\hat{\boldsymbol{P}}$ as the electron linear momentum operator. We stress that the wavefunction in Eq. (5) is an *electronic* wavefunction only, which has a parametric dependence on the nuclear coordinates, indicated by the superscript $(\boldsymbol{r}_A, \boldsymbol{r}_B, \boldsymbol{R})$.

Here, we point out two aspects of the electronic wavefunction which are implicit in the notation of Eq. (5). First of all, the electronic wavefunction is anti-symmetric with respect to the exchange of any two electrons, which is accomplished by acting on Eq. (5) with the anti-symmetrizer

$$\hat{\mathcal{A}} = \frac{1}{N!}\sum_{\hat{P}\in S_N}(-1)^p\hat{P}. \tag{6}$$

Here, N is the total number of electrons, S_N is the symmetric group of order N, and p is the parity of the permutation $\hat{P}$. Second, the spin sub-state is implicit above, and a more explicit notation may be

$$\begin{aligned}|\psi_A\psi_B\rangle^{(\boldsymbol{r}_A,\boldsymbol{r}_B,\boldsymbol{R})} = \hat{\mathcal{A}}\sum_{M_A,M_B}&\left[\hat{\mathcal{T}}(-\boldsymbol{R}/2)\hat{\mathcal{R}}(\boldsymbol{r}_A)|\psi_A(0,0,0)S_AM_A\rangle\right]\\ &\otimes\left[\hat{\mathcal{T}}(\boldsymbol{R}/2)\hat{\mathcal{R}}(\boldsymbol{r}_B)|\psi_B(0,0,0)S_BM_B\rangle\right]\\ &\times\langle S_AM_AS_BM_B|SM\rangle,\end{aligned} \tag{7}$$

where $\langle S_AM_AS_BM_B|SM\rangle$ is a Clebsch-Gordan coefficient that serves to couple the monomer spin angular momenta to a total S with projection M onto the space-fixed z-axis. For the triplet states considered in this work, $S = 1, M = -1, 0, 1$, and the value of S_A (S_B) depends on the monomer state of molecule A (B). As noted above, the rotation operators do not act on the electron spin coordinates. If they would, and hence rotate the spin states of both monomers over different angles, the wavefunction in Eq. (7) would not necessarily be a pure triplet state. The spin state plays no role except for determining certain symmetry properties and in the calculation of the spin-orbit coupling, required in the diabatization procedure. Therefore, we will mostly use the implicit and more compact notation of Eq. (5).

Also for interacting monomers, the adiabatic wavefunctions can be approximated by a linear combination of products of rotated monomer states,

$$|\Psi_a^{(\text{adiabatic})}\rangle^{(\boldsymbol{r}_A,\boldsymbol{r}_B,\boldsymbol{R})} \approx \sum_{\psi_A,\psi_B}|\psi_A\psi_B\rangle^{(\boldsymbol{r}_A,\boldsymbol{r}_B,\boldsymbol{R})}U_{\psi_A,\psi_B;a}(\boldsymbol{r}_A,\boldsymbol{r}_B,\boldsymbol{R}), \tag{8}$$

where a labels the adiabatic states and $U_{\psi_A,\psi_B;a}$ is an element of the unitary transformation between adiabatic states and the products of rotated monomer wavefunctions. Within this space of wavefunctions, the products of rotated monomer wavefunctions minimize non-adiabatic coupling and therefore serve as a quasi-diabatic basis. We will now discuss how this transformation between the adiabatic and quasi-diabatic representations is determined from one-electron properties.

In order to evaluate one-electron properties in the diabatic basis, we write any one-electron operator as a direct sum of monomer one-electron property operators,

$$\hat{O} = \hat{O}^{(A)}\otimes\hat{1}^{(B)} + \hat{1}^{(A)}\otimes\hat{O}^{(B)}, \tag{9}$$

where $\hat{1}^{(X)}$ is the identity operator for the electronic coordinates of monomer $X = A, B$. Matrix elements in the diabatic basis are then given by

$$\langle\psi_A\psi_B|\hat{O}|\psi'_A\psi'_B\rangle^{(\boldsymbol{r}_A,\boldsymbol{r}_B,\boldsymbol{R})} = \langle\psi_A|\hat{\mathcal{R}}(0,\theta_A,0)^\dagger\hat{\mathcal{T}}(-\boldsymbol{R}/2)^\dagger\hat{O}^{(A)}\hat{\mathcal{T}}(-\boldsymbol{R}/2)\hat{\mathcal{R}}(0,\theta_A,0)|\psi'_A\rangle\delta_{\psi_B,\psi'_B} + \delta_{\psi_A,\psi'_A}\langle\psi_B|\hat{\mathcal{R}}(\phi,\theta_B,0)^\dagger\hat{\mathcal{T}}(\boldsymbol{R}/2)^\dagger\hat{O}^{(B)}\hat{\mathcal{T}}(\boldsymbol{R}/2)\hat{\mathcal{R}}(\phi,\theta_B,0)|\psi'_B\rangle. \quad (10)$$

We note that in our short-hand notation for the nuclear coordinates in Eq. (10), the superscript $(\boldsymbol{r}_A,\boldsymbol{r}_B,\boldsymbol{R})$ applies to both bra and ket as well as to the one-electron operator, $\hat{O}$. The translated one-electron properties of the form $\hat{\mathcal{T}}^\dagger\hat{O}\hat{\mathcal{T}}$ can be obtained analytically, but in many cases, this shift of origin does not have to be considered explicitly, for example, because the lowest non-vanishing multipole moments are origin independent. If the one-electron property is the qth component of a rank-k spherical tensor operator, denoted as $\hat{O}^{(k)}_q$, we can also perform the rotation analytically to obtain

$$\langle\psi|\hat{\mathcal{R}}^\dagger\hat{O}^{(k)}_q\hat{\mathcal{R}}|\psi'\rangle = \sum_{q'}\langle\psi|\hat{O}^{(k)}_{q'}|\psi'\rangle D^{(k)}_{q',q}(\hat{\mathcal{R}}^{-1}), \quad (11)$$

where $D^{(k)}_{mq}(\hat{\mathcal{R}}) = \langle km|\hat{\mathcal{R}}|kq\rangle$ denotes a Wigner D-matrix element depending on the Euler angles of the rotation $\hat{\mathcal{R}}$. This last equation gives the required matrix elements completely in terms of the transition moments between the monomer states, $\langle\psi|\hat{O}^{(k)}_{q'}|\psi\rangle$, as obtained in an electronic structure calculation for a single monomer in the monomer-fixed frame, as described at the beginning of this section.

Above, it is explained how we calculate one-electron properties in the diabatic representation. These properties are also calculated in the adiabatic representation as expectation values and transition moments between wavefunctions from *ab initio* calculations, as implemented in many electronic structure packages. In this way, we obtain all components of the orbital angular momentum and of the electric quadrupole operators in both representations. The transformation from the adiabatic to the diabatic representation is then fit to these properties as described in Ref. 9 and briefly explained below. The transformation $\boldsymbol{U}$ should satisfy

$$\boldsymbol{U}\boldsymbol{A}_p - \boldsymbol{D}_p\boldsymbol{U} = \boldsymbol{0}, \quad (12)$$

where $\boldsymbol{A}_p$ is a matrix representation of a property, labeled by p, in the adiabatic basis, and $\boldsymbol{D}_p$ is a representation of the same property in the diabatic basis. This equation is linear in each element of $\boldsymbol{U}$ and hence can be vectorized to yield

$$\begin{aligned}\boldsymbol{M}_p\mathrm{vec}(\boldsymbol{U}) &= \boldsymbol{0},\\ \boldsymbol{M}_p &= \boldsymbol{A}_p^T\otimes\boldsymbol{1} - \boldsymbol{1}\otimes\boldsymbol{D}_p.\end{aligned} \quad (13)$$

Now we seek the non-trivial $\boldsymbol{U}$ that minimizes

$$\sum_p w_p||\boldsymbol{U}\boldsymbol{A}_p - \boldsymbol{D}_p\boldsymbol{U}||^2, \quad (14)$$

i.e., that minimizes the square norm of the residual of Eq. (12) averaged with weights w_p over an arbitrary number of properties. The solution for $\mathrm{vec}(\boldsymbol{U})$ is found as the eigenvector at zero eigenvalue of the matrix

$$\sum_p w_p\boldsymbol{M}_p^\dagger\boldsymbol{M}_p. \quad (15)$$

The matrix $\boldsymbol{U}$ is then found by appropriately reshaping this eigenvector. Furthermore, we set mixing between the energetically well-separated states correlating to different asymptotes to zero and impose unitarity on the resulting $\boldsymbol{U}$ through a singular value decomposition, as explained in Ref. 9.

The precise choice of weights, w_p, in Eq. (15) should not have a strong influence on the calculated transformation, but its inclusion is necessary in order to include different properties which may have different units. The weights are typically chosen such that each term in Eq. (15) is dimensionless and roughly of the same magnitude.

Each term in the sum over the properties in Eq. (15) is positive semi-definite and hence can only increase all eigenvalues of the matrix. Therefore, properties can be added until the degeneracy of the lowest eigenvalue is lifted, and the solution for $\boldsymbol{U}$ is uniquely determined. Inclusion of the electric quadrupole moment and orbital angular momentum both with weights $w_p = 1$ a.u. is not sufficient to accomplish this, as we obtain two independent solutions that differ only in the sign of the contributions of excitations localized on monomers A and B. To resolve this issue, we compute the spin-orbit coupling given both possible transformations and compare this with the spin-orbit coupling calculated in the adiabatic representation. This spin-orbit coupling exists between the state correlating to $O_2(X^3\Sigma_g^-) - O_2(X^3\Sigma_g^-)$ and the two states correlating to $O_2(X^3\Sigma_g^-) - O_2(b^1\Sigma_g^+)$. Although the energetically well-separated $X^3\Sigma_g^- - X^3\Sigma_g^-$ state does not mix with the other states, its inclusion in the diabatization procedure is very useful, as this allows determining the relative phases that affect the sign of the transition dipole moments.

The spin-orbit coupling in the diabatic representation is calculated as follows. We use an approach similar to the one above, in Eq. (10), except that the operator involved is now a spin-dependent scalar operator,

$$\langle\psi_A\psi_B|\hat{H}_{\mathrm{SO}}|\psi'_A\psi'_B\rangle^{(\boldsymbol{r}_A,\boldsymbol{r}_B,\boldsymbol{R})} = \sum_{M_A,M_B,M'_A,M'_B}\Big[\langle\psi_A S_A M_A|\hat{\mathcal{R}}(0,\theta_A,0)^\dagger\hat{H}^{(A)}_{\mathrm{SO}}\hat{\mathcal{R}}(0,\theta_A,0)|\psi'_A S'_A M'_A\rangle\delta_{\psi_B,\psi'_B} + \delta_{\psi_A,\psi'_A}\langle\psi_B S_B M_B|\hat{\mathcal{R}}(\phi,\theta_B,0)^\dagger\hat{H}^{(B)}_{\mathrm{SO}}\hat{\mathcal{R}}(\phi,\theta_B,0)|\psi'_B S'_B M'_B\rangle\Big]\langle S_A M_A S_B M_B|SM\rangle\langle S'_A M'_A S'_B M'_B|S'M'\rangle. \quad (16)$$

Because $\hat{H}_{\mathrm{SO}}$ is invariant under simultaneous rotations of the electronic spin and spatial coordinates, we find for rotations of spatial coordinates only

$$\hat{\mathcal{R}}(\boldsymbol{r})^{\dagger}\hat{H}_{\mathrm{SO}}\hat{\mathcal{R}}(\boldsymbol{r}) = \hat{\mathcal{R}}^{\mathrm{spin}}(\boldsymbol{r})\hat{H}_{\mathrm{SO}}\hat{\mathcal{R}}^{\mathrm{spin}}(\boldsymbol{r})^{\dagger}. \tag{17}$$

Thus, we obtain for the matrix elements on the right-hand side of Eq. (16)

$$\begin{aligned}
&\langle \psi SM|\hat{\mathcal{R}}^{\mathrm{spin}}(\boldsymbol{r})\hat{H}_{\mathrm{SO}}\hat{\mathcal{R}}^{\mathrm{spin}}(\boldsymbol{r})^{\dagger}|\psi' S'M'\rangle \\
&\quad = \sum_{\mu,\mu'} D^{(S)}_{\mu,M}(\mathcal{R}^{-1})D^{(S')}_{\mu',M'}(\mathcal{R}^{-1})\langle \psi S\mu|\hat{H}_{\mathrm{SO}}|\psi' S'\mu'\rangle \\
&\quad = \sum_{\mu,\mu',\alpha,\beta,\gamma} D^{(\alpha)}_{\beta,\gamma}(\mathcal{R}^{-1})\langle S\mu S'\mu'|\alpha\beta\rangle\langle SMS'M'|\alpha\gamma\rangle \\
&\qquad \times \langle \psi S\mu|\hat{H}_{\mathrm{SO}}|\psi' S'\mu'\rangle.
\end{aligned} \tag{18}$$

The spin-orbit coupling between $X^3\Sigma_g^-$ and $b^1\Sigma_g^+$ of O_2 is denoted as $\langle\psi|\hat{H}_{\mathrm{SO}}|\psi'\rangle$ for the case $\mu = \mu' = 0$ and vanishes otherwise. The Clebsch-Gordan coefficients can be simplified by noting that for the non-vanishing contributions, one of S_A, S'_A, S_B, and S'_B equals 0 and the remaining three quantum numbers equal 1. This yields

$$\begin{aligned}
&\langle \psi SM|\hat{\mathcal{R}}^{\mathrm{spin}}(\boldsymbol{r})\hat{H}_{\mathrm{SO}}\hat{\mathcal{R}}^{\mathrm{spin}}(\boldsymbol{r})^{\dagger}|\psi' S'M'\rangle \\
&\quad = D^{(1)}_{0,M+M'}(\mathcal{R}^{-1})\langle\psi|\hat{H}_{\mathrm{SO}}|\psi'\rangle,
\end{aligned} \tag{19}$$

and we obtain for the spin-orbit coupling in the diabatic model

$$\begin{aligned}
&\langle \psi_A\psi_B|\hat{H}_{\mathrm{SO}}|\psi'_A\psi'_B\rangle^{(\boldsymbol{r}_A,\boldsymbol{r}_B,\boldsymbol{R})} \\
&\quad = D^{(1)}_{0,M'-M}(0,-\theta_A,0)\langle 1,\ M'-M,\ 1, M|1,M'\rangle \\
&\qquad \times \langle\psi_A|\hat{H}_{\mathrm{SO}}|\psi'_A\rangle + D^{(1)}_{0,M'-M}(0,-\theta_B,-\phi_B) \\
&\qquad \times \langle 1,M,1,\ M'-M\ |1,M'\rangle\langle\psi_B|\hat{H}_{\mathrm{SO}}|\psi'_B\rangle.
\end{aligned} \tag{20}$$

B. Expansion of the diabatic potential energy surfaces

In this section, we consider the expansion of the diabatic potential energy surfaces in angular functions and derive constraints on the expansion from symmetry relations. This derivation is similar to what is presented in Ref. 26, which treats diabatic potentials for two open-shell diatomic molecules. However, the present derivation uses a rotation-operator formalism which avoids the definition of two-angle and three-angle embedded frames. Furthermore, we also consider couplings between different monomer electronic states, rather than only between the sub-levels of the same electronic state. The expansion of the transition dipole moment surfaces is considered in Sec. II C. The results presented here reduce to those of Ref. 26 in the special cases of diagonal potentials and off-diagonal potentials that couple the spatially degenerate sub-levels of the same monomer states.

We again consider two diatoms, A and B, with internuclear axes $\boldsymbol{r}_A$ and $\boldsymbol{r}_B$, and intermolecular axis $\boldsymbol{R}$, all with respect to some arbitrary space-fixed reference frame. A matrix element of the electronic Hamiltonian $\hat{\mathcal{H}}$ is an analytic function of these angles and can be expanded in products of complex-conjugated Wigner D-matrix elements, $D^{(l)*}_{m,k}(\phi_X,\theta_X,0)$, and Racah-normalized spherical harmonics, $C_{L,M}(\Theta,\Phi)$. Exploiting the rotational invariance of $\hat{\mathcal{H}}$, this general angular expansion can be compactified by Clebsch-Gordan coupling the angular functions to a scalar, yielding

$$\begin{aligned}
&\langle \psi_{A,\Lambda_A}\psi_{B,\Lambda_B}|\hat{\mathcal{H}}|\psi'_{A,\Lambda'_A}\psi'_{B,\Lambda'_B}\rangle^{(\boldsymbol{r}_A,\boldsymbol{r}_B,\boldsymbol{R})} \\
&\quad = \sum_{L_A,L_B,L} \mathcal{V}_{L_A,L_B,L}^{\psi_{A,\Lambda_A},\psi_{B,\Lambda_B},\psi'_{A,\Lambda'_A},\psi'_{B,\Lambda'_B}}(R) \\
&\qquad \times \sum_{M_A,M_B,M} \langle L_AM_AL_BM_B|LM\rangle\langle L,M,L,\ -M|00\rangle \\
&\qquad \times D^{(L_A)*}_{M_A,\Lambda_A-\Lambda'_A}(\phi_A,\theta_A,0)D^{(L_B)*}_{M_B,\Lambda_B-\Lambda'_B}(\phi_B,\theta_B,0) \\
&\qquad \times C_{L,-M}(\Theta,\Phi).
\end{aligned} \tag{21}$$

We note again that our superscript short-hand notation for the nuclear coordinates applies to the entire bracket, i.e., to both bra, ket, and also to the electronic Hamiltonian, which has a parametric dependence on the nuclear coordinates. The above expansion of the interaction matrix element in a complete basis of functions of the angles is exact but not unique. The presented form of the expansion has the advantage that it smoothly approaches the correct asymptotic form for large R,[26] where electrostatic long-range interactions contribute, see Sec. II D.

In the *ab initio* calculations, we use the dimer-fixed reference frame with monomer A in the xz-plane, i.e., $\phi_A = \Theta = \Phi = 0$. In this case, the matrix element of the interaction operator takes the form

$$\begin{aligned}
&\langle \psi_{A,\Lambda_A}\psi_{B,\Lambda_B}|\hat{\mathcal{H}}|\psi'_{A,\Lambda'_A}\psi'_{B,\Lambda'_B}\rangle^{(\boldsymbol{r}_A,\boldsymbol{r}_B,\boldsymbol{R})} \\
&\quad = \sum_{L_A,L_B,L} \mathcal{V}_{L_A,L_B,L}^{\psi_{A,\Lambda_A},\psi_{B,\Lambda_B},\psi'_{A,\Lambda'_A},\psi'_{B,\Lambda'_B}}(R) \\
&\qquad \times \sum_{M} \langle L_A,\ -M, L_B, M|L0\rangle\langle L0L0|00\rangle \\
&\qquad \times d^{(L_A)}_{-M,\Lambda_A-\Lambda'_A}(\theta_A)d^{(L_B)}_{M,\Lambda_B-\Lambda'_B}(\theta_B)\exp(iM\phi_B).
\end{aligned} \tag{22}$$

Using the orthogonality of the angular functions,

$$\begin{aligned}
&\int_{-1}^{1} d^{(L)}_{M,K}(\theta)d^{(L')}_{M,K}(\theta)\, d\cos(\theta) = \frac{2}{2L+1}\delta_{L,L'}, \\
&\int_0^{2\pi} \exp(-iM'\phi)\exp(iM\phi)\, d\phi = 2\pi\delta_{M,M'},
\end{aligned} \tag{23}$$

one can obtain the expansion coefficients by numerical integration,

$$\begin{aligned}
\mathcal{V}_{L_A,L_B,M}^{\psi_{A,\Lambda_A},\psi_{B,\Lambda_B},\psi'_{A,\Lambda'_A},\psi'_{B,\Lambda'_B}} &= \frac{(2L_A+1)(2L_B+1)}{8\pi} \\
&\quad \times \int e^{-iM\phi} d^{(L_A)}_{-M,\Lambda_A-\Lambda'_A}(\theta_A)d^{(L_B)}_{M,\Lambda_B-\Lambda'_B}(\theta_B) \\
&\quad \times \langle \psi_A\psi_B|\hat{\mathcal{H}}|\psi'_A\psi'_B\rangle^{(\boldsymbol{r}_A,\boldsymbol{r}_B,\boldsymbol{R})} \\
&\quad \times d\cos(\theta_A)\, d\cos(\theta_B)\, d\phi,
\end{aligned}$$

$$\begin{aligned}
\mathcal{V}_{L_A,L_B,L}^{\psi_{A,\Lambda_A},\psi_{B,\Lambda_B},\psi'_{A,\Lambda'_A},\psi'_{B,\Lambda'_B}} &= \sum_M \mathcal{V}_{L_A,L_B,M}^{\psi_{A,\Lambda_A},\psi_{B,\Lambda_B},\psi'_{A,\Lambda'_A},\psi'_{B,\Lambda'_B}} \\
&\quad \times \frac{\langle L_A,\ -M, L_B, M|L0\rangle}{\langle L0L0|00\rangle}.
\end{aligned} \tag{24}$$

It is convenient to evaluate the above integral numerically using Gauss-Legendre quadrature points in $\cos(\theta)$ and a Gauss-Chebyshev quadrature in $\cos(\phi)$.

Rotational invariance of the Hamiltonian is already exploited to simplify the expansion of the interaction by Clebsch-Gordan coupling the angular functions to a scalar operator, but further symmetries can be used to place additional constraints on the expansion coefficients. In Subsection 1 of the Appendix, we derive restrictions on the expansion coefficients of the diabatic potential energy surfaces, Eq. (21), from inversion symmetry (25a), hermiticity of the electronic Hamiltonian (25b), time reversal (25c), and permutation of identical nuclei (25d–25f). The resulting relations are summarized as follows:

$$\mathcal{V}^{\psi_{A,\Lambda_A},\psi_{B,\Lambda_B},\psi'_{A,\Lambda'_A},\psi'_{B,\Lambda'_B}}_{L_A,L_B,L} = (-1)^{L_A+L_B+L} \times \mathcal{V}^{\psi_{A,-\Lambda_A},\psi_{B,-\Lambda_B},\psi'_{A,-\Lambda'_A},\psi'_{B,-\Lambda'_B}}_{L_A,L_B,L}, \tag{25a}$$

$$\mathcal{V}^{\psi_{A,\Lambda_A},\psi_{B,\Lambda_B},\psi'_{A,\Lambda'_A},\psi'_{B,\Lambda'_B}}_{L_A,L_B,L} = (-1)^{L_A+L_B+L} \times \left(\mathcal{V}^{\psi'_{A,\Lambda'_A},\psi'_{B,\Lambda'_B},\psi_{A,\Lambda_A},\psi_{B,\Lambda_B}}_{L_A,L_B,L}\right)^*, \tag{25b}$$

$$\mathcal{V}^{\psi_{A,\Lambda_A},\psi_{B,\Lambda_B},\psi'_{A,\Lambda'_A},\psi'_{B,\Lambda'_B}}_{L_A,L_B,L} = (-1)^{L_A+L_B+L} \times \left(\mathcal{V}^{\psi_{A,-\Lambda_A},\psi_{B,-\Lambda_B},\psi'_{A,-\Lambda'_A},\psi'_{B,-\Lambda'_B}}_{L_A,L_B,L}\right)^*, \tag{25c}$$

$$\mathcal{V}^{\psi_{A,\Lambda_A},\psi_{B,\Lambda_B},\psi'_{A,\Lambda'_A},\psi'_{B,\Lambda'_B}}_{L_A,L_B,L} = (-1)^{L_A+\rho_{\psi_A}+\rho_{\psi'_A}} \times \mathcal{V}^{\psi_{A,-\Lambda_A},\psi_{B,\Lambda_B},\psi'_{A,-\Lambda'_A},\psi'_{B,\Lambda'_B}}_{L_A,L_B,L}, \tag{25d}$$

$$\mathcal{V}^{\psi_{A,\Lambda_A},\psi_{B,\Lambda_B},\psi'_{A,\Lambda'_A},\psi'_{B,\Lambda'_B}}_{L_A,L_B,L} = (-1)^{L_B+\rho_{\psi_B}+\rho_{\psi'_B}} \times \mathcal{V}^{\psi_{A,\Lambda_A},\psi_{B,-\Lambda_B},\psi'_{A,\Lambda'_A},\psi'_{B,-\Lambda'_B}}_{L_A,L_B,L}, \tag{25e}$$

$$\mathcal{V}^{\psi_{A,\Lambda_A},\psi_{B,\Lambda_B},\psi'_{A,\Lambda'_A},\psi'_{B,\Lambda'_B}}_{L_A,L_B,L} = (-1)^{L_A+L_B} \times \mathcal{V}^{\psi_{B,\Lambda_B},\psi_{A,\Lambda_A},\psi'_{B,\Lambda'_B},\psi'_{A,\Lambda'_A}}_{L_B,L_A,L}, \tag{25f}$$

where ρ_ψ is the phase obtained under the action of σ_{xz} for monomer state ψ, defined in Eq. (A5).

From the symmetry under inversion, Eq. (25a), and time reversal, Eq. (25c), we conclude that all expansion coefficients are real valued. From Eq. (25b) we then find that $L_A + L_B + L$ must be even for all diagonal potentials and for potentials involving only Σ states. Combining (25a), (25d), and (25e), valid for homonuclear diatomic monomers, we find that L is even in all cases. For potentials involving Σ states, there are constraints on L_A and L_B individually: for diagonal potentials, only even L_A and even L_B occur, whereas for the off-diagonal potential coupling $|X^3\Sigma_g^- b^1\Sigma_g^+\rangle$ with $|b^1\Sigma_g^+ X^3\Sigma_g^-\rangle$, only odd L_A and odd L_B occur. For diagonal potentials involving one Σ state and one $\Lambda \neq 0$ state, combining Eqs. (25a), (25d), and (25e) shows that L_A, L_B, and L are all even. However, for off-diagonal potentials involving $\Lambda_X \neq 0$ states, there are no general constraints on the parity of L_X.

C. Expansion of the dipole moment surfaces

We now consider the expansion of the dipole moment surfaces in terms of complex conjugated Wigner D-matrix elements and Racah-normalized spherical harmonics. This proceeds largely analogous to the potential energy surfaces, except that the dipole operator is not invariant under rotations. Rather, it transforms as a vector operator with three spherical components related to the usual Cartesian components as $\hat{\mu}_{\pm1} = \mp(\mu_x \pm i\mu_y)/\sqrt{2}$ and $\hat{\mu}_0 = \hat{\mu}_z$. This suggests the expansion in Clebsch-Gordan coupled angular functions as

$$\begin{aligned}\langle\psi_{A,\Lambda_A}\psi_{B,\Lambda_B}|\hat{\mu}_\nu|\psi'_{A,\Lambda'_A}\psi'_{B,\Lambda'_B}\rangle^{(\boldsymbol{r}_A,\boldsymbol{r}_B,\boldsymbol{R})} &= \sum_{L_A,L_B,\lambda,L} \mathcal{D}^{\psi_{A,\Lambda_A},\psi_{B,\Lambda_B},\psi'_{A,\Lambda'_A},\psi'_{B,\Lambda'_B}}_{L_A,L_B,\lambda,L}(R) \\ &\times \sum_{M_A,M_B,\mu,M} \langle L_A M_A L_B M_B|\lambda\mu\rangle\langle\lambda\mu LM|1\nu\rangle \\ &\times D^{(L_A)*}_{M_A,\Lambda_A-\Lambda'_A}(\phi_A,\theta_A,0) D^{(L_B)*}_{M_B,\Lambda_B-\Lambda'_B}(\phi_B,\theta_B,0) \\ &\times C_{L,M}(\Theta,\Phi).\end{aligned} \tag{26}$$

As was done for the potential, we consider how to determine the expansion coefficients from matrix elements calculated at suitably chosen geometries. The dipole moment in the dimer-fixed frame is given by

$$\begin{aligned}\langle\psi_{A,\Lambda_A}\psi_{B,\Lambda_B}|\hat{\mu}_\nu|\psi'_{A,\Lambda'_A}\psi'_{B,\Lambda'_B}\rangle^{(\boldsymbol{r}_A,\boldsymbol{r}_B,\boldsymbol{R})} &= \sum_{L_A,L_B,\lambda,L} \mathcal{D}^{\psi_{A,\Lambda_A},\psi_{B,\Lambda_B},\psi'_{A,\Lambda'_A},\psi'_{B,\Lambda'_B}}_{L_A,L_B,\lambda,L}(R) \\ &\times \sum_M \langle L_A,\ \nu-M,\ L_B, M|\lambda\nu\rangle\langle\lambda\nu L0|1\nu\rangle \\ &\times d^{(L_A)}_{\nu-M,\Lambda_A-\Lambda'_A}(\theta_A) d^{(L_B)}_{M,\Lambda_B-\Lambda'_B}(\theta_B)\exp(iM\phi_B).\end{aligned} \tag{27}$$

Using again the orthogonality relations, Eq. (23), one may obtain the expansion coefficients as follows:

$$\begin{aligned}\mathcal{D}^{\psi_{A,\Lambda_A},\psi_{B,\Lambda_B},\psi'_{A,\Lambda'_A},\psi'_{B,\Lambda'_B}}_{L_A,L_B,M,\nu} &= \frac{(2L_A+1)(2L_B+1)}{8\pi}\int e^{-iM\phi} d^{(L_A)}_{\nu-M,\Lambda_A-\Lambda'_A}(\theta_A) \\ &\times d^{(L_B)}_{M,\Lambda_B-\Lambda'_B}(\theta_B)\langle\psi_A\psi_B|\hat{\mu}_\nu|\psi'_A\psi'_B\rangle^{(\boldsymbol{r}_A,\boldsymbol{r}_B,\boldsymbol{R})} \\ &\times d\cos(\theta_A)\, d\cos(\theta_B)\, d\phi,\end{aligned}$$

$$\mathcal{D}^{\psi_{A,\Lambda_A},\psi_{B,\Lambda_B},\psi'_{A,\Lambda'_A},\psi'_{B,\Lambda'_B}}_{L_A,L_B,M,\nu} = \sum_{\lambda,L} \mathcal{D}^{\psi_{A,\Lambda_A},\psi_{B,\Lambda_B},\psi'_{A,\Lambda'_A},\psi'_{B,\Lambda'_B}}_{L_A,L_B,\lambda,L} \times \langle L_A,\ \nu-M,\ L_B, M|\lambda\nu\rangle\langle\lambda\nu L0|1\nu\rangle. \tag{28}$$

These integrals can be evaluated accurately using the same Gauss-Legendre quadrature in $\cos(\theta)$ and Gauss-Chebyshev quadrature in $\cos(\phi)$ as were used for the potential.

Again, we derive relations between the expansion coefficients from symmetry operations. The derivations can be

found in Subsection 2 of the Appendix, and the results are summarized as follows:

$$\mathcal{D}^{\psi_{A,\Lambda_A},\psi_{B,\Lambda_B},\psi'_{A,\Lambda'_A},\psi'_{B,\Lambda'_B}}_{L_A,L_B,\lambda,L} = (-1)^{L_A+L_B+L} \times \mathcal{D}^{\psi_{A,-\Lambda_A},\psi_{B,-\Lambda_B},\psi'_{A,-\Lambda'_A},\psi'_{B,-\Lambda'_B}}_{L_A,L_B,\lambda,L}, \quad (29a)$$

$$\mathcal{D}^{\psi_{A,\Lambda_A},\psi_{B,\Lambda_B},\psi'_{A,\Lambda'_A},\psi'_{B,\Lambda'_B}}_{L_A,L_B,\lambda,L} = (-1)^{L_A+L_B+L+1} \times \left(\mathcal{D}^{\psi'_{A,\Lambda'_A},\psi'_{B,\Lambda'_B},\psi_{A,\Lambda_A},\psi_{B,\Lambda_B}}_{L_A,L_B,\lambda,L}\right)^*, \quad (29b)$$

$$\mathcal{D}^{\psi_{A,\Lambda_A},\psi_{B,\Lambda_B},\psi'_{A,\Lambda'_A},\psi'_{B,\Lambda'_B}}_{L_A,L_B,\lambda,L} = (-1)^{L_A+L_B+L+1} \times \left(\mathcal{D}^{\psi_{A,-\Lambda_A},\psi_{B,-\Lambda_B},\psi'_{A,-\Lambda'_A},\psi'_{B,-\Lambda'_B}}_{L_A,L_B,\lambda,L}\right)^*, \quad (29c)$$

$$\mathcal{D}^{\psi_{A,\Lambda_A},\psi_{B,\Lambda_B},\psi'_{A,\Lambda'_A},\psi'_{B,\Lambda'_B}}_{L_A,L_B,\lambda,L} = (-1)^{L_A+\rho_{\psi_A}+\rho_{\psi'_A}} \times \mathcal{D}^{\psi_{A,-\Lambda_A},\psi_{B,\Lambda_B},\psi'_{A,-\Lambda'_A},\psi'_{B,\Lambda'_B}}_{L_A,L_B,\lambda,L}, \quad (29d)$$

$$\mathcal{D}^{\psi_{A,\Lambda_A},\psi_{B,\Lambda_B},\psi'_{A,\Lambda'_A},\psi'_{B,\Lambda'_B}}_{L_A,L_B,\lambda,L} = (-1)^{L_B+\rho_{\psi_B}+\rho_{\psi'_B}} \times \mathcal{D}^{\psi_{A,\Lambda_A},\psi_{B,-\Lambda_B},\psi'_{A,\Lambda'_A},\psi'_{B,-\Lambda'_B}}_{L_A,L_B,\lambda,L}, \quad (29e)$$

$$\mathcal{D}^{\psi_{A,\Lambda_A},\psi_{B,\Lambda_B},\psi'_{A,\Lambda'_A},\psi'_{B,\Lambda'_B}}_{L_A,L_B,\lambda,L} = (-1)^{L_A+L_B+\lambda+L+1} \times \mathcal{D}^{\psi_{B,\Lambda_B},\psi_{A,\Lambda_A},\psi'_{B,\Lambda'_B},\psi'_{A,\Lambda'_A}}_{L_B,L_A,\lambda,L}, \quad (29f)$$

where again the phase ρ_ψ is defined in Eq. (A5). These results are derived from inversion symmetry (29a), hermiticity of the dipole operator (29b), time reversal (29c), and permutation of identical nuclei (29d)–(29f).

Combining the results obtained from the symmetry under inversion, Eq. (29a), and time reversal, Eq. (29c), we conclude that all expansion coefficients are purely imaginary. We note that if we were considering expectation values rather than transition dipole moments, all expansion coefficients would have been real valued, as in this case $\rho_{\psi_A}+\rho_{\psi_B}+\rho_{\psi'_A}+\rho_{\psi'_B}$ is even, opposite to what is assumed in the present derivation of Eq. (29a). From Eq. (29c), we also see that the expansion coefficients for transitions involving only Σ states must have L_A+L_B+L even. For these transitions, L_A (L_B) is odd and L_B (L_A) is even, for the case where molecule A (B) is carrying the excitation. Combining Eq. (29c) with Eqs. (29d) and (29e), we see that L is odd in all cases.

D. Multipole expansion

The Coulomb operator describing the long-range electrostatic interaction between monomers A and B can be expanded in a multipole series as

$$\hat{H}_{\rm el} = \sum_{l_A l_B M_{AB}} \frac{(-1)^{l_B}}{R^{l_A+l_B+1}} \begin{pmatrix} 2l_A+2l_B \\ 2l_A \end{pmatrix}^{1/2} \langle l_A m_A l_B m_B | l_A+l_B,\, m_A+m_B\rangle \times \hat{Q}^{(A)}_{l_A,m_A} \hat{Q}^{(B)}_{l_B,m_B} C^*_{l_A+l_B,m_A+m_B}(\hat{R}), \quad (30)$$

where the symbol in parentheses is a binomial coefficient, and $\hat{Q}^{(X)}_{l_X,m_X}$ denotes the m_X spherical component of the 2^{l_X}-pole operator for monomer $X=A, B$.[27,28]

The first-order interaction is obtained by taking matrix elements of Eq. (30) between products of undistorted monomer wavefunctions, Eq. (5). This yields Eq. (21), where the expansion coefficients are given by their first-order form

$$\mathcal{V}^{\psi_{A,\Lambda_A},\psi_{B,\Lambda_B},\psi'_{A,\Lambda'_A},\psi'_{B,\Lambda'_B}}_{L_A,L_B,L} = \delta_{L_A+L_B,L} \frac{(-1)^{L_A}\sqrt{2L+1}}{R^{L+1}} \begin{pmatrix} 2L_A+2L_B \\ 2L_A \end{pmatrix}^{1/2} \times \langle \psi_{A,\Lambda_A} | \hat{Q}_{L_A,\Lambda_A-\Lambda'_A} | \psi'_{A,\Lambda'_A}\rangle \times \langle \psi_{B,\Lambda_B} | \hat{Q}_{L_B,\Lambda_B-\Lambda'_B} | \psi'_{B,\Lambda'_B}\rangle. \quad (31)$$

Non-vanishing contributions correspond to non-zero (transition) multipole moments on the monomers. Furthermore, using the inversion symmetry of the monomers, multipole moments may be shown to vanish for odd L_X. Finally, many of the off-diagonal potentials in this work can be shown to vanish because the monomer functions $|\psi_X\rangle$ and $|\psi'_X\rangle$ correspond to different electronic spins.

The second-order interaction is obtained by calculating matrix elements of

$$\hat{H}^{(2)} = \hat{H}_{\rm el}\hat{G}\hat{H}_{\rm el}, \qquad \hat{G} = \sum_{\psi_A\psi_B}{}' \frac{|\psi_A\psi_B\rangle\langle\psi_A\psi_B|}{\Delta E_{\psi_A}+\Delta E_{\psi_B}}, \quad (32)$$

where ΔE_{ψ_X} is the excitation energy for the excitation from the state of interest to $|\psi_X\rangle$, for monomer $X=A, B$. As indicated by the primed sum, the reduced resolvent, $\hat{G}$, contains a sum over all states, excluding terms for which the denominator vanishes. Terms with $\Delta E_{\psi_A}=0$ or $\Delta E_{\psi_B}=0$ give rise to induction interactions, and the terms with both $\Delta E_{\psi_A}\neq 0$ and $\Delta E_{\psi_B}\neq 0$ give rise to dispersion. With some rearrangements,[28] the second-order interaction operator is given by[29]

$$\hat{H}^{(2)} = -\sum_{l_A l_B l'_A l'_B p_A p_B p_{AB} q_{AB}} \frac{f^{(p_A p_B p_{AB})}_{l_1 l_2 l'_1 l'_2} C^*_{p_{AB},q_{AB}}(\hat{R})}{R^{l_A+l_B+l'_A+l'_B+2}} \sum_{\psi_A\psi_B}{}' \frac{\left[\left[\hat{Q}_{l_A}|\psi_A\rangle\langle\psi_A|\hat{Q}_{l'_A}\right]^{(p_A)} \otimes \left[\hat{Q}_{l_B}|\psi_B\rangle\langle\psi_B|\hat{Q}_{l'_B}\right]^{(p_B)}\right]^{(p_{AB})}_{q_{AB}}}{\Delta E_a+\Delta E_b}, \quad (33)$$

with the coefficients $f^{(p_A p_B p_{AB})}_{l_A l_B l'_A l'_B}$ given by Eq. (21) of Ref. 28. Following Casimir and Polder,[30] the following relation can be used to write each spherical term as a product of operators for monomers A and B:

$$\frac{1}{A+B} = \frac{1}{2\pi}\int_0^\infty \frac{2A}{A^2+\omega^2}\frac{2B}{B^2+\omega^2}d\omega. \quad (34)$$

Taking matrix elements of Eq. (33) yields terms proportional to products of transition moments of the form

$\langle\psi_X|\hat{Q}_{L,M}|\psi''_X\rangle\langle\psi''_X|\hat{Q}_{L',M'}|\psi'_X\rangle$, summed over the doubly primed intermediate states. Generally speaking, these contributions never vanish due to symmetry, except when $|\psi_X\rangle$ and $|\psi'_X\rangle$ correspond to different electronic spins. For the diagonal potential, these contributions can be related to frequency-dependent polarizabilities of the monomers.

The interaction-induced dipole moment can be computed in the long-range from electrostatic perturbation theory as well.[31] As the interaction potential in the above derivation, the interaction-induced dipole is related to the molecular multipole moments and polarizabilities. For *diagonal* dipole moments, important contributions are quadrupole-induced dipole moments, varying as R^{-4}, hexadecapole-induced moments, varying with R^{-6}, and dispersion contributions, varying with R^{-7}. However, for the important transition dipole moments in this work, connecting the $X^3\Sigma_g^-$ ground state with the singlet excited states, *all* long-range contributions vanish because the monomer electronic spin is not conserved.

III. BENCHMARK *AB INITIO* CALCULATIONS

In this section, we report benchmark calculations for the potential energy and dipole moment surfaces. We study the convergence with respect to the one-electron basis set and the dependence on the level of electron correlation. These calculations are performed for highly symmetric orientations of the molecules. The high symmetry is exploited to speed up the calculation, such that we can perform tests which would otherwise become prohibitively expensive. Furthermore, the high symmetry simplifies the calculation as in many cases the quasi-degenerate excited states carry different irreducible representations, thus removing their non-adiabatic coupling. Finally, the direction of the transition dipole moments is determined by symmetry, which simplifies the comparison and interpretation of these moments.

We define three choices of the active space as follows:

- The small Complete Active Space (sCAS) contains four electrons in the four π^* orbitals. This is the minimal active space that allows for a zeroth-order description of all states of interest, i.e., all states corresponding to the $(\pi)^4(\pi^*)^2$ electronic configuration of the O_2 monomers.
- The medium Complete Active Space (mCAS) contains 12 electrons in the π-shell. This active space can describe the static correlation of the π electrons. This is important for O_2, as is well-known from studies of the Hartree-Fock instability of O_2, associated with artificial breaking of inversion symmetry.[32]
- The large Complete Active Space (ℓCAS) contains 16 electrons in the p-shell.

Calculations with the ℓCAS are prohibitively expensive at low symmetry geometries, and therefore calculations of the full potential energy and dipole moment surfaces are not feasible using this active space.

A. Interaction energy

We first consider the H-shaped geometry ($\theta_A = \theta_B = \pi/2$ and $\phi = 0$) at an intermolecular separation $R = 6\ a_0$. This separation corresponds to the minimum of the potential for the triplet $O_2(X^3\Sigma_g^-) - O_2(X^3\Sigma_g^-)$ state.[19] Table I shows the interaction energies for the seven triplet states of interest using explicitly correlated multi-reference configuration interaction with Davidson's size-consistency correction (F12-MRCI+Q) using three choices for the active space[33] as well as the mCAS F12-CASPT2 method.[34] The augmented correlation consistent basis sets (aug-cc-pVnZ, where n = D, T, Q is the cardinality) were used,[35] together with the standardized auxiliary basis sets of Refs. 36 and 37. We used Slater-type geminals with exponent $\gamma_{12} = 1\ a_0^{-1}$ in the explicitly correlated treatment, which is the MOLPRO default parameter setting, and we have deviated from the defaults only in the use of more stringent thresholds. The remaining size-consistency error was corrected for by subtracting the interaction energy at $R = 100\ a_0$, and the basis-set superposition error was corrected for by a counterpoise scheme described in Sec. IV.

The dependence of the MRCI results on the choice of active space is substantial, but we may expect reasonably converged interaction energies using the mCAS active space. The root-mean-square deviation from the larger ℓCAS calculation is 8 cm^{-1} or less than 10% of the well depth, using the same triple zeta basis set in both calculations. The difference

TABLE I. Interaction energies in cm^{-1} for all seven triplet states at the H-shaped geometry.

State	aug-cc-pVDZ	aug-cc-pVTZ	aug-cc-pVQZ
sCAS F12-MRCI+Q			
$A_g\ X^3\Sigma_g^- - a^1\Delta_g$	−68.27	−40.78	−32.13
$B_{2u}\ X^3\Sigma_g^- - a^1\Delta_g$	−96.71	−72.44	−65.13
$B_{2u}\ X^3\Sigma_g^- - b^1\Sigma_g^+$	−98.16	−73.62	−65.61
$B_{1u}\ X^3\Sigma_g^- - X^3\Sigma_g^-$	−149.46	−124.95	−116.20
$B_{1u}\ X^3\Sigma_g^- - a^1\Delta_g$	−162.75	−136.59	−127.75
$B_{3g}\ X^3\Sigma_g^- - a^1\Delta_g$	−127.71	−104.22	−96.85
$B_{3g}\ X^3\Sigma_g^- - b^1\Sigma_g^+$	−135.92	−111.71	−103.71
mCAS F12-MRCI+Q			
$A_g\ X^3\Sigma_g^- - a^1\Delta_g$	−64.94	−39.53	−31.65
$B_{2u}\ X^3\Sigma_g^- - a^1\Delta_g$	−93.78	−70.66	−63.57
$B_{2u}\ X^3\Sigma_g^- - b^1\Sigma_g^+$	−95.49	−71.89	−64.23
$B_{1u}\ X^3\Sigma_g^- - X^3\Sigma_g^-$	−148.54	−125.32	−117.63
$B_{1u}\ X^3\Sigma_g^- - a^1\Delta_g$	−159.08	−135.21	−127.21
$B_{3g}\ X^3\Sigma_g^- - a^1\Delta_g$	−124.85	−102.63	−95.50
$B_{3g}\ X^3\Sigma_g^- - b^1\Sigma_g^+$	−132.52	−109.26	−101.63
ℓCAS F12-MRCI+Q			
$A_g X^3\Sigma_g^- - a^1\Delta_g$	−73.44	−46.73	
$B_{2u} X^3\Sigma_g^- - a^1\Delta_g$	−102.72	−78.47	
$B_{2u} X^3\Sigma_g^- - b^1\Sigma_g^+$	−105.01	−80.55	
$B_{1u} X^3\Sigma_g^- - X^3\Sigma_g^-$	−157.83	−133.40	
$B_{1u} X^3\Sigma_g^- - a^1\Delta_g$	−169.79	−144.87	
$B_{3g} X^3\Sigma_g^- - a^1\Delta_g$	−134.73	−111.40	
$B_{3g} X^3\Sigma_g^- - b^1\Sigma_g^+$	−143.15	−119.12	
mCAS F12-CASPT2			
$A_g X^3\Sigma_g^- - a^1\Delta_g$	−50.26	−33.61	−37.83
$B_{2u} X^3\Sigma_g^- - a^1\Delta_g$	−89.87	−73.16	−76.64
$B_{2u} X^3\Sigma_g^- - b^1\Sigma_g^+$	−92.31	−76.11	−79.85
$B_{1u} X^3\Sigma_g^- - X^3\Sigma_g^-$	−156.03	−139.36	−142.42
$B_{1u} X^3\Sigma_g^- - a^1\Delta_g$	−167.92	−152.53	−156.16
$B_{3g} X^3\Sigma_g^- - a^1\Delta_g$	−130.32	−114.36	−117.66
$B_{3g} X^3\Sigma_g^- - b^1\Sigma_g^+$	−140.34	−124.67	−128.25

TABLE II. Non-zero transition dipole moments involving the $B_{1u}X^3\Sigma_g^- - X^3\Sigma_g^-$ triplet ground state at the H-shaped geometry in units of mea_0.

Method	Final state basis set	$A_g\ X^3\Sigma_g^- - a^1\Delta_g$	$B_{3g}\ X^3\Sigma_g^- - a^1\Delta_g$	$B_{3g}\ X^3\Sigma_g^- - b^1\Sigma_g^+$
sCAS CASSCF	aug-cc-pVDZ	0.1595	0.2952	0.0184
	aug-cc-pVTZ	0.1572	0.3169	0.0141
	aug-cc-pVQZ	0.1552	0.3152	0.0139
mCAS CASSCF	aug-cc-pVDZ	0.1771	0.2350	0.0126
	aug-cc-pVTZ	0.1729	0.2547	0.0089
	aug-cc-pVQZ	0.1710	0.2531	0.0088
ℓCAS CASSCF	aug-cc-pVDZ	0.1843	0.2413	0.0076
	aug-cc-pVTZ	0.1797	0.2635	0.2635
sCAS MRCI	aug-cc-pVDZ	0.2264	0.6049	0.0873
	aug-cc-pVTZ	0.2090	0.5581	0.0711
	aug-cc-pVQZ	0.1997	0.5395	0.0676
mCAS MRCI	aug-cc-pVDZ	0.2536	0.5534	0.1045
	aug-cc-pVTZ	0.2295	0.5052	0.0837
	aug-cc-pVQZ	0.2198	0.4867	0.0790
ℓCAS MRCI	aug-cc-pVDZ	0.2871	0.6312	0.1174
	aug-cc-pVTZ	0.2528	0.5584	0.0919

with the mCAS CASPT2 result can, assuming that the conclusions of Ref. 18 also apply to the excited states, be used as a more conservative estimate of the accuracy of the interaction energy. The root-mean-square deviation between mCAS F12-MRCI+Q and mCAS F12-CASPT2 results, both in aug-cc-pVTZ, is about 13 cm^{-1} or 11% of the well depth. The results converge smoothly with the quality of the one-electron basis set, and triple-ζ basis sets yield results converged to about 7 cm^{-1}.

B. Transition dipole moments

Here, we report transition dipole moments at the CASSCF and MRCI levels of theory, using different active spaces and one-electron basis sets. Non-zero transition dipole moments for the H-shaped geometry ($\theta_A = \theta_B = \pi/2$, $\phi = 0$, and $R = 6\ a_0$) are shown in Table II. The transition dipole moment converges smoothly with the one-electron basis set, and reasonably converged results are obtained with triple-ζ basis sets. However, there are large discrepancies between CASSCF and MRCI calculations. Differences between calculations with different choices of the active space are smaller but also significant. We may conclude from Table II that the interaction-induced transition dipole moments are very small. This may be an important reason why it is difficult to obtain converged results for this property.

We have performed further exploratory calculations at the T-shaped ($\theta_A = \pi/2$, $\theta_B = \phi = 0$, and $R = 7\ a_0$) and X-shaped ($\theta_A = \theta_B = \phi = \pi/2$ and $R = 6\ a_0$) geometries, as well as for shorter separations, for which the transition dipole moments are much larger, as they decay roughly with an exponential R-dependence. In absolute sense, the dipole moments remain small and very sensitive to the level at which electron correlation is treated. This is rather surprising for a one-electron property such as the dipole moment. The apparent sensitivity to electron correlation also seems to be at odds with the smooth convergence with respect to the one-electron basis set. However, it should be stressed that the interaction-induced dipole moments, considered here, do not correspond to simple one-electron excitations, which may result in the reported sensitivity to electron correlation.

Ultimately, we cannot convincingly draw any conclusions about the accuracy of either method for computing the weak interaction-induced electronic transition dipole moments. Therefore, we decide to compute global dipole moment surfaces at both the mCAS CASSCF and the mCAS MRCI levels. Both approaches are commonly used methods, and the difference between the two surfaces may be useful for indicating the uncertainty of our results.

IV. COMPUTATIONAL DETAILS

A. Methodology

Based on the benchmark calculations described above, we decided to use the explicitly correlated multi-reference configuration interaction method in an aug-cc-pVTZ basis set to compute potential energy and dipole moment surfaces. Here, we summarize the details of the calculations of these global surfaces. The dipole moment surface is also reported at the CASSCF level of theory. In this case, the same calculations were performed, except that the configuration interaction step was omitted.

All *ab initio* calculations were carried out with the MOLPRO 2012 package.[38] Molecular orbitals were calculated in complete active space self-consistent field (CASSCF) calculations, using the mCAS active space described above, which contains 12 electrons in the 8 orbitals correlating to the O_2 π-shell. State-averaged calculations were performed including all nearly degenerate states correlating to the same asymptote, i.e., separate sets of orbitals were used for the $X^3\Sigma_g^- - X^3\Sigma_g^-$ state, four states correlating to $X^3\Sigma_g^- - a^1\Delta_g$,

and two states correlating to $X^3\Sigma_g^- - b^1\Sigma_g^+$. Next, dynamic correlation was treated by performing F12-MRCI+Q calculations, in which again the coupling between the nearly degenerate states was included. Interaction energies were calculated including Davidson's size-consistency correction. The residual size-consistency error was corrected for by subtracting the interaction energy at $R = 10\,000\ a_0$, and the basis-set superposition error (BSSE) was corrected for by the generalized counterpoise procedure reported below.

Transition moments between the configuration-interaction wavefunctions are calculated for the dipole and quadrupole moments, as well as for the orbital angular momentum operator. Calculation of these transition moments between wavefunctions defined with different orbitals requires a transformation to biorthogonal orbitals. This is currently not implemented for spin-orbit matrix elements; hence, we cannot directly compute the spin-orbit coupling between the $X^3\Sigma_g^- - X^3\Sigma_g^-$ ground state and the two excited states correlating to $X^3\Sigma_g^- - b^1\Sigma_g^+$. Instead, we recompute the ground state wavefunction with the orbitals optimized for the excited state and use this wavefunction to calculate the spin-orbit coupling required for the diabatization procedure. We correct the spin-orbit matrix elements for a possible phase difference between the ground-state wavefunctions calculated with both sets of orbitals. This phase difference is determined by calculating the overlap of the ground state wavefunctions computed using both sets of orbitals. For computing the wavefunction overlap, the transformation to biorthogonal orbitals is implemented in MOLPRO 2012.

B. Counterpoise procedure

Interaction energies and other interaction-induced properties which are calculated from electronic structure calculations for the dimer contain the basis-set superposition error (BSSE). This error is reduced by subtracting the monomer energies or properties evaluated in the dimer basis set. For closed-shell monomers, this is called the counterpoise procedure of Boys and Bernardi.[39] For open-shell fragments, the procedure is not uniquely defined, as the degenerate monomer sub-states yield different counterpoise corrections in the dimer basis set.

For two interacting open-shell atoms, a generalized counterpoise procedure has been proposed where the contributions of different monomer sub-states to the adiabatic states are estimated from the asymptotic wavefunction.[40,41] In the present work, we determine the contributions of different monomer sub-states to each adiabatic state by the diabatization procedure, and we could correct the diabatic potential energy surfaces accordingly. Instead, we opt for the simpler approach of calculating counterpoise corrections by averaging the monomer energies over excitations localized on either monomer and over the two spatial components of the Δ state. To be explicit, we correct the potential for the state correlating to $O_2(X^3\Sigma_g^-) - O_2(X^3\Sigma_g^-)$ as

$$V_{X^3\Sigma_g^- X^3\Sigma_g^-}(\hat{\boldsymbol{r}}_A, \hat{\boldsymbol{r}}_B, R) = E^{(AB)}_{X^3\Sigma_g^- - X^3\Sigma_g^-}(\hat{\boldsymbol{r}}_A, \hat{\boldsymbol{r}}_B, R) - E^{(A)}_{X^3\Sigma_g^-}(\hat{\boldsymbol{r}}_A, \hat{\boldsymbol{r}}_B, R) - E^{(B)}_{X^3\Sigma_g^-}(\hat{\boldsymbol{r}}_A, \hat{\boldsymbol{r}}_B, R), \tag{35}$$

we correct potentials for the four states correlating to $O_2(X^3\Sigma_g^-) - O_2(a^1\Delta_g)$ as

$$\begin{aligned} V_{X^3\Sigma_g^- - a^1\Delta_g}(\hat{\boldsymbol{r}}_A, \hat{\boldsymbol{r}}_B, R) &= E^{(AB)}_{X^3\Sigma_g^- - a^1\Delta_g}(\hat{\boldsymbol{r}}_A, \hat{\boldsymbol{r}}_B, R) - \frac{1}{2}E^{(A)}_{X^3\Sigma_g^-}(\hat{\boldsymbol{r}}_A, \hat{\boldsymbol{r}}_B, R) \\ &\quad - \frac{1}{4}E^{(A)}_{a^1\Delta_{xy}}(\hat{\boldsymbol{r}}_A, \hat{\boldsymbol{r}}_B, R) - \frac{1}{4}E^{(A)}_{a^1\Delta_{x^2-y^2}}(\hat{\boldsymbol{r}}_A, \hat{\boldsymbol{r}}_B, R) \\ &\quad - \frac{1}{2}E^{(B)}_{X^3\Sigma_g^-}(\hat{\boldsymbol{r}}_A, \hat{\boldsymbol{r}}_B, R) - \frac{1}{4}E^{(B)}_{a^1\Delta_{xy}}(\hat{\boldsymbol{r}}_A, \hat{\boldsymbol{r}}_B, R) \\ &\quad - \frac{1}{4}E^{(B)}_{a^1\Delta_{x^2-y^2}}(\hat{\boldsymbol{r}}_A, \hat{\boldsymbol{r}}_B, R), \end{aligned} \tag{36}$$

and for the two states correlating to $O_2(X^3\Sigma_g^-) - O_2(b^1\Sigma_g^+)$ as

$$\begin{aligned} V_{X^3\Sigma_g^- - b^1\Sigma_g^+}(\hat{\boldsymbol{r}}_A, \hat{\boldsymbol{r}}_B, R) &= E^{(AB)}_{X^3\Sigma_g^- - b^1\Sigma_g^+}(\hat{\boldsymbol{r}}_A, \hat{\boldsymbol{r}}_B, R) - \frac{1}{2}E^{(A)}_{X^3\Sigma_g^-}(\hat{\boldsymbol{r}}_A, \hat{\boldsymbol{r}}_B, R) \\ &\quad - \frac{1}{2}E^{(A)}_{b^1\Sigma_g^+}(\hat{\boldsymbol{r}}_A, \hat{\boldsymbol{r}}_B, R) - \frac{1}{2}E^{(B)}_{X^3\Sigma_g^-}(\hat{\boldsymbol{r}}_A, \hat{\boldsymbol{r}}_B, R) \\ &\quad - \frac{1}{2}E^{(B)}_{b^1\Sigma_g^+}(\hat{\boldsymbol{r}}_A, \hat{\boldsymbol{r}}_B, R), \end{aligned} \tag{37}$$

where E is the adiabatic energy calculated in the dimer-centered one-electron basis set, the superscript denotes a dimer calculation (AB) or a specific monomer (A or B), and the subscript denotes the electronic state.

The differences between the BSSE corrections for different sub-states are small in any case, below 1 cm^{-1} near the H-shaped minimum, but the present approach–apart from being simpler–has the advantage of applying the same correction to each member of a set of asymptotically degenerate states. This means that the position of the seams of conical intersections is unaffected by the BSSE correction and that the adiabatic potentials are consistent with the transformation to the diabatic basis.

Finally, we note that we cannot correct transition dipole moments for the BSSE, as the monomer transition dipole moments to be subtracted always vanish because the transition is spin-forbidden.

C. Geometries

For the angular coordinates, we use 10-point Gauss-Legendre quadratures in $\cos(\theta_A)$ and $\cos(\theta_B)$ and a 10-point equidistant grid in ϕ, which can be thought of as a Gauss-Chebyshev quadrature in $\cos(\phi)$. Using the permutation-inversion symmetry of identical nuclei allows us to restrict the angles θ_A and θ_B to values between 0 and $\pi/2$ with $\theta_A \geq \theta_B$ and to restrict ϕ to the range $[0,\pi]$. In total, this amounts to 150 unique orientations. The transformations relating these geometries are in Subsection 1 of the Appendix. These operations were used to transform properties, i.e., orbital angular momenta, dipole, and quadrupole moments, to determine their values at symmetry-equivalent geometries not explicitly included in the grid. The monomer vibrational coordinates are kept fixed at $r_A = r_B = 2.28\ a_0$. The radial grid consists of the points $R = 5.5$, 5.75, 6, 6.25, 6.5, 6.75, 7, 7.25, 7.5, 8, 8.5, 9, 9.5, 10, 12, 15, and 20 a_0. Including an additional point at

$R = 10\,000\ a_0$ to correct for a size-consistency error, this amounts to 2700 geometries.

V. INTERPOLATION METHOD

The calculations outlined above yield diabatic potential energy and dipole moment surfaces on the quadrature points in the angles θ_A, θ_B, and ϕ and on a discrete grid in the separation, R. For a fixed value of R, we obtain the expansion coefficients of these surfaces by numerical integration over the angles, using Eqs. (24) and (28). To obtain truly global energy and dipole surfaces, the expansion coefficients have to be fit as a function of R. A popular method for this purpose is the reproducing kernel Hilbert space (RKHS).[42] At short separations, this method smoothly interpolates between the *ab initio* points, whereas RKHS extrapolates to asymptotically large separations as R^{-n}, where the exponent is conveniently chosen to coincide with the leading term from long-range theory. RKHS extrapolation to short separations is polynomial, even though an exponential R-dependence may be more appropriate. Also, exponential extrapolation for large separations is more realistic for the monomer-spin-changing off-diagonal potentials and transition dipole moments, which vanish at all orders in electrostatic long-range theory. Therefore, we propose a new method for interpolating *ab initio* points with exponential extrapolation to both small and large separations.

The aim is to find a function $y(R)$ that interpolates the expansion coefficients of the potential energy surfaces and the transition dipole moment surfaces, y_i, in the radial grid points, R_i, for $i = 1, \ldots, N$. The basic idea is to write the expansion coefficient as a linear combination of functions of R where there are as many functions, and therefore linear fit parameters, as *ab initio* points,

$$y(R) = \sum_{i=1}^{N} c_i f_i(R). \tag{38}$$

We choose to use one unique function centered at each of the *ab initio* points,

$$f_i(R) = f(R - R_i). \tag{39}$$

In this way, there are sufficient parameters to have the fit pass exactly through all of the data points, i.e., it will interpolate the *ab initio* points. The extrapolatory behavior is determined by the asymptotic form of the fit functions, which we would like to be

$$y(R) \propto \exp(-\alpha_0 R) \qquad \text{for } R \ll R_1, \tag{40}$$

$$y(R) \propto \exp(-\alpha_\infty R) \qquad \text{for } R \gg R_N. \tag{41}$$

Therefore, we choose to use

$$f_i(R) = \exp\left\{-\left[R - R_i\right]\phi(R - R_i)\right\}, \tag{42}$$

$$\phi(x) = \frac{\alpha_\infty + \alpha_0}{2} + \frac{\alpha_\infty - \alpha_0}{2\pi}\tan^{-1}\left(\frac{x}{\lambda}\right), \tag{43}$$

that is, $f_i(R)$ is exponential for distances much shorter or much larger than R_i, and around R_i, the exponent switches from α_0 to α_∞ on a length scale set by λ.

We define a matrix $\boldsymbol{F}$, with elements

$$F_{i,j} = f_j(R_i), \tag{44}$$

the column vector $\boldsymbol{y}$, which contains the expansion coefficient to be interpolated, y_i, and the vector $\boldsymbol{c}$, which contains the linear fit parameters, c_i. The fit parameters that exactly interpolate the *ab initio* points satisfy

$$\boldsymbol{F}\boldsymbol{c} = \boldsymbol{y}. \tag{45}$$

If the fit functions are linearly independent, the matrix $\boldsymbol{F}$ can be inverted and the system solved for the fit parameters

$$\boldsymbol{c} = \boldsymbol{F}^{-1}\boldsymbol{y}. \tag{46}$$

If the fit functions become numerically linearly dependent, a regularized solution can be obtained by using the pseudo-inverse

$$\boldsymbol{F}^{-1} \approx \boldsymbol{R}(\boldsymbol{\Sigma} + \nu \boldsymbol{1}_{N\times N})^{-1}\boldsymbol{L}^\dagger, \tag{47}$$

where

$$\boldsymbol{F} = \boldsymbol{L}\boldsymbol{\Sigma}\boldsymbol{R}^\dagger \tag{48}$$

is the singular value decomposition of $\boldsymbol{F}$, i.e., the columns of the unitary matrices $\boldsymbol{L}$ and $\boldsymbol{R}$ contain the left and right singular vectors, respectively, and $\boldsymbol{\Sigma}$ is a diagonal matrix whose entries are called the singular values. Choosing $\nu = \max(\boldsymbol{\Sigma}) \times 10^{-10} = \Sigma_{1,1} \times 10^{-10}$ ensures that the inverse of the diagonal matrix in Eq. (47) can be safely evaluated, and subsequently, the pseudo-inverse of $\boldsymbol{F}$ is obtained by numerically accurate multiplications by unitary matrices.

A. Fitting strategy for the potential energy surfaces

We consider fitting the radial dependence of an expansion coefficient of the potential energy surface, $\mathcal{V}^{\psi_{A,\Lambda_A},\psi_{B,\Lambda_B},\psi'_{A,\Lambda'_A},\psi'_{B,\Lambda'_B}}_{L_A,L_B,L}(R)$. We first determine whether this term has long-range contributions from first-order electrostatics or second-order dipole-dipole dispersion. Long-range interactions are present only for the diagonal potentials and for off-diagonal potentials that couple $\pm\Lambda$ sub-states of the same monomer state, i.e., where $\psi_A = \psi'_A$ and $\psi_B = \psi'_B$ but $\Lambda_A = -\Lambda'_A$ or $\Lambda_B = -\Lambda'_B$. Long-range interactions vanish at all orders for off-diagonal potentials that couple the excitations localized on different monomers because the monomer electron spin is not conserved. First-order interactions occur for $L_A, L_B > 0$ and $L_A + L_B = L$ and vary as R^{-n} with $n = L + 1$. In practice, we consider only first-order interactions involving the quadrupole and hexadecapole moments, $L_A, L_B = 2, 4$. Second-order dipole-dipole dispersion, varying with R^{-6}, contributes to terms with $L_A, L_B \leq 2$ and L_A, L_B, and L satisfying the triangular conditions.

If long-range interactions are present, these are fit in an R^m-weighted linear least squares fit to

$$y_{lr}(R) = \sum_n c_n R^{-n} \tag{49}$$

where m is determined by the leading term in the long-range interaction. This fit is performed using *ab initio* points for $R > 10\ a_0$. Next, we obtain the damped long-range potential by multiplication with a Tang-Toennies damping function,

$$V_{lr}(R) = \sum_n c_n f_{n,\beta}(R) R^{-n},$$
$$f_{n,\beta}(R) = 1 - \exp(-\beta R)\sum_{k=0}^{n}\frac{(\beta R)^k}{k!}, \tag{50}$$

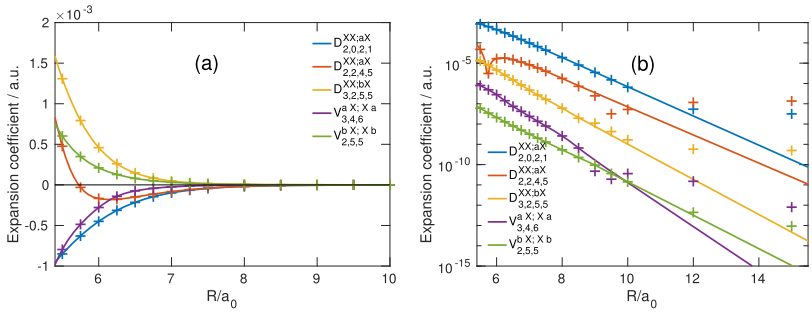

FIG. 1. The fitting procedure for a few expansion terms of the diabatic potential energy and dipole moment surfaces. (a) shows the expansion coefficients on a linear scale, whereas (b) shows their absolute values on a logarithmic scale. Lines in (b) have been shifted vertically for clarity. Markers indicate the *ab initio* points and lines indicate the exponential interpolation. The exponential interpolation and extrapolation scheme interpolates the data in the short range, where the expansion coefficients vary roughly exponentially with separation, R. At larger separations, the exponential fit decays below a noise level and the data points are left out of the analysis, as explained in the main text.

with $\beta = 2.0\ a_0^{-1}$. This damped long-range potential is evaluated in the radial grid points, $R_i, i = 1, \ldots, N$, and subtracted from the *ab initio* points. The remainder is by definition the short-range potential and is fit as described below.

The short-range potential is fit, for $R \leq 10\ a_0$, using the exponential interpolation scheme described above. The fit functions are defined by an inner and outer exponent, α_0 and α_∞, and a length scale, λ, for which we choose

$$\lambda = \sqrt{1 + \frac{2}{\sqrt{5}}} \tag{51}$$

in atomic units. This choice of the length scale ensures that the exponent switches smoothly from 80% α_0 to 80% α_∞ between $\pm 1\ a_0$ around the grid point. In order to obtain smooth fit functions, the exponent cannot change too much over the fixed length scale. Therefore, we set $\alpha_0 = \alpha_\infty + 0.1$ a.u., i.e., the inner exponential function is slightly steeper. The value of α_∞ is determined by the asymptotic behavior as described below.

The outer exponent is determined by the actual asymptotic behavior of the short-range potential. To this end, we first determine whether the short-range potential actually decays exponentially at the outermost three grid points considered. This is the case if the short-range potential has the same sign at these grid points, and if so, if the logarithm of the absolute value of the potential is a linear function of R in this range. To determine whether this is a linear function, we perform a linear least squares fit to the form $aR + b$ and accept if the residual sum of squares is sufficiently small if $\mathbb{R}^2 > 0.975$. This coefficient of determination is defined as

$$\mathbb{R}^2 = 1 - \frac{\mathrm{Var}[\boldsymbol{y} - (a\boldsymbol{R} + b)]}{\mathrm{Var}(\boldsymbol{y})}, \tag{52}$$

where the variance is

$$\mathrm{Var}(\boldsymbol{x}) = \sum_i (x_i - \bar{x})^2. \tag{53}$$

The exponent obtained from this fit is used as the outer exponent, α_∞, in the interpolation scheme. In practice, we see that much larger $\mathbb{R}^2 \approx 0.99$ are often obtained, and this is typically the case unless the short-range potential has decayed below the noise level of numerical accuracy at the last grid points. Therefore, if the short-range potential is not found to decay exponentially, we decrease the range used in the fit by removing the grid point at the largest value of R and attempt again to fit the three outermost data points with a single exponent. This process is repeated until an exponential decay is found.

In some cases, the data range has been reduced manually. Also, to avoid inaccuracy when extrapolating to shorter separations, some insignificant contributions have been removed altogether, as they rose above the noise level in too few grid points to determine whether they actually should be extrapolated exponentially.

B. Fitting strategy for the dipole moment surfaces

The fitting strategy for the dipole moment surfaces is very similar to that for the potential energy surfaces. A difference is that the asymptotically spin-forbidden transition dipole moments considered in this work have no R^{-n} long-range form, and therefore only the short-range exponential interpolation scheme is employed. A second difference is that the range of *ab initio* points used in this fit was decreased to all points at $R \leq 8\ a_0$ because the asymptotically forbidden transition dipole moments are much smaller and hardly exceed the noise level for larger separations. Because of the inherent smallness of the dipole moments, it much more frequently occurred that the fit range had to be adjusted manually or that terms had to be omitted.

Figure 1 illustrates the typical fitting procedure. The procedure determines a short-range region in which the expansion coefficients vary exponentially with separation. These *ab initio* points, and those at yet shorter separations, are interpolated by the scheme outlined above. At larger separations, the exponential fit decays below a noise level and the data points are not used for interpolation. This is clearly visible in particular in panel (b), which shows the absolute value of the expansion coefficients on a logarithmic scale. In this panel, successive lines have been shifted down by powers of 10 for the clarity of the figure.

VI. NUMERICAL RESULTS

A. Global diabatic potential energy surfaces

The global potential energy surfaces are shown in Fig. 2 for H-shaped geometries ($\theta_A = \theta_B = \pi/2$, $\phi = 0$), relative to the

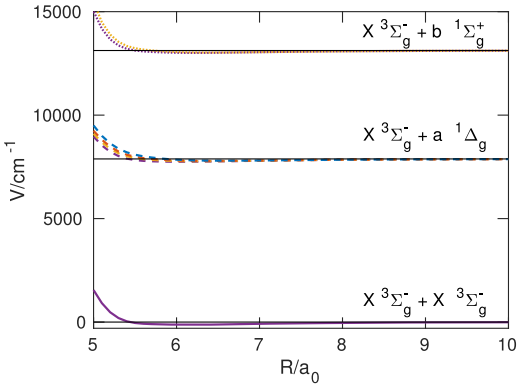

FIG. 2. The calculated F12-MRCI+Q potentials for H-shaped geometries ($\theta_A = \theta_B = \pi/2$, $\phi = 0$) as a function of the inter-molecular separation, R. Solid black lines mark the lowest three asymptotes, as indicated, and the remaining lines represent the adiabatic electronic states, where different colors distinguish between different electronic states correlating to the same asymptote.

lowest asymptote. The triplet ground-state of the complex correlates to the lowest asymptote, $O_2(X^3\Sigma_g^-) - O_2(X^3\Sigma_g^-)$, four asymptotically degenerate electronic states correlate to the second asymptote at 7883 cm^{-1}, $O_2(X^3\Sigma_g^-) - O_2(a^1\Delta_g)$, and two further electronic states correlate to the third asymptote at 13 122 cm^{-1}, $O_2(X^3\Sigma_g^-) - O_2(b^1\Sigma_g^+)$. States correlating to the different asymptotes remain well separated for all relevant separations, whereas the asymptotically degenerate state correlating to the same asymptotes remain close in energy for all separations. The well depths are small compared to the asymptotic energy difference, and therefore the shape of the potential wells and their differences are not clearly visible in Fig. 2. In what follows, we will therefore subtract the asymptotic energy difference.

The shifted global potential energy surfaces are shown in Fig. 3. This figure shows the adiabatic potential energy for fixed four orientations as a function of the intermolecular distance, R. The adiabatic energies have been obtained by evaluating the fit diabatic potential energies, followed by diagonalization of the diabatic potential energy matrix. The potential for the triplet ground state is shown as the solid line, the potentials for states correlating to the $O_2(X^3\Sigma_g^-)$ – $O_2(a^1\Delta_g)$ asymptote are shown as the dashed lines, and potentials for states correlating to $O_2(X^3\Sigma_g^-)$ – $O_2(b^1\Sigma_g^+)$ are represented by the dotted lines. Different colors correspond to different adiabatic states correlating to the same asymptote.

As can be seen from Fig. 3, the splitting between the adiabatic states correlating to each asymptote is relatively small, at most tens of wave numbers near the H-shaped minima. The potentials for states correlating to electronically excited O_2 moieties are generally very similar to those for the triplet ground state, as for fixed orientations, all states exhibit minima at roughly the same positions and depth. The differences are even smaller if we consider only the isotropic part of the potential, i.e., the $L_A = L_B = L = 0$ term in Eq. (21), shown in Fig. 4. This means that the orientational average of the potential is very similar for all states, but the anisotropy is slightly different for each electronic state. The reason for the similarity of the potentials is that the electronic configuration is identical for all monomer electronic states considered.

We have also compared the present potential for the triplet ground to those of Ref. 19, which was obtained by combining a quintet CCSD(T) potential with exchange splittings computed using MRCI. The comparison is shown in Fig. 5, where the present results are shown as solid lines and the results from Ref. 19 are shown as dashed lines, with different colors corresponding to different orientations. We qualitatively find good agreement between the two potentials, although the present potential is somewhat less attractive. This might have been expected as dispersion is described more accurately at the CCSD(T) level. The isotropic parts of these potentials, shown as the black lines in Fig. 5, can be brought in closer agreement by increasing the isotropic dispersion coefficient, $c^{(6)}_{0,0,0}$, by 27% such that it matches the recommended value of Ref. 43. The remaining fit parameters are kept unchanged. The resulting fit is shown as the dotted line in Fig. 5. With this scaling, the two isotropic potentials differed by no more than

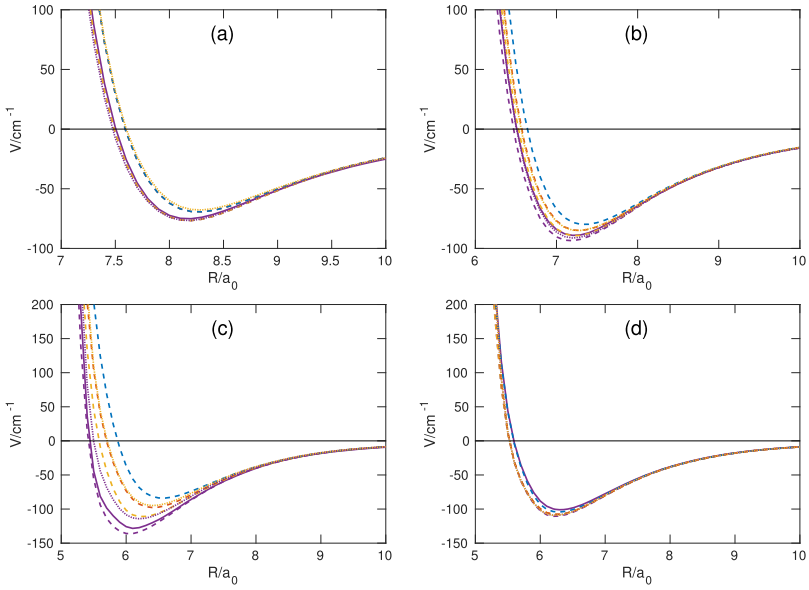

FIG. 3. The R-dependence of the adiabatic potential energy surface for fixed orientations. (a) through (d) refer to collinear ($\theta_A = \theta_B = 0$), T-shaped ($\theta_A = 0$, $\theta_B = \pi/2$), H-shaped ($\theta_A = \theta_B = \pi/2$, $\phi = 0$), and X-shaped ($\theta_A = \theta_B = \phi = \pi/2$), respectively. The solid line corresponds to the triplet ground state, the dotted lines correlate to $O_2(X^3\Sigma_g^-)$ – $O_2(a^1\Delta_g)$, and the dashed lines correlate to $O_2(X^3\Sigma_g^-)$ – $O_2(b^1\Sigma_g^+)$. Different colors distinguish adiabatic states correlating to the same asymptote.

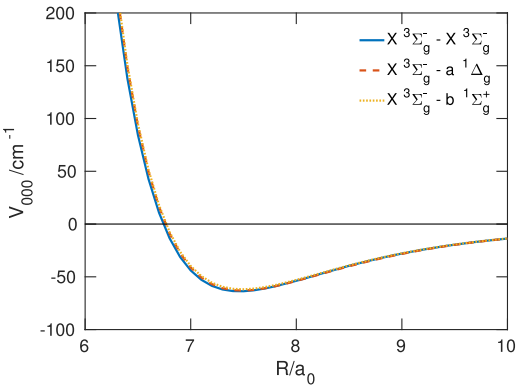

FIG. 4. Isotropic component of the potential energy surfaces for each asymptote as a function of the separation.

6 cm^{-1} for the most relevant separations, $R > 6\ a_0$. Although this scaling does not bring the full orientation-dependent potentials in close agreement, applying such a scaling may be useful for sampling the sensitivity of subsequent dynamical calculations to the uncertainty in the potential, especially for dynamical calculations employing the isotropic potential only, such as the calculations reported in Paper II.[44]

B. Global dipole moment surfaces

Global transition dipole moments are shown in Fig. 6. All geometries are coplanar, $\phi = 0$, and the transitions shown have the transition dipole moment perpendicular to the plane of the complex. Shown as the solid and dashed-dotted lines are the results obtained at the MRCI and CASSCF levels of theory, respectively. It is clear that there are substantial differences between the dipole surfaces obtained using these two approaches, which may not be a surprise after the exploratory calculations reported in Sec. III and the numerical study in Ref. 23. We cannot make claims about the accuracy to which either of these dipole moment surfaces is converged, so the difference between the two may serve to indicate the large uncertainty in the calculation of such properties.

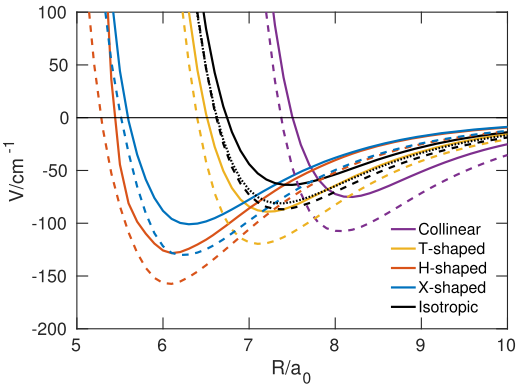

FIG. 5. The potentials from the present work and Ref. 19 as the solid and dashed lines, respectively. The different colors correspond to collinear ($\theta_A = \theta_B = 0$), T-shaped ($\theta_A = 0$, $\theta_B = \pi/2$), H-shaped ($\theta_A = \theta_B = \pi/2$, $\phi = 0$), and X-shaped ($\theta_A = \theta_B = \phi = \pi/2$) orientations as indicated. The black lines show the isotropic potential, for which an additional dotted line is included, corresponding to the present isotropic potential with scaled $c^{(6)}_{0,0,0}$, as explained in the text.

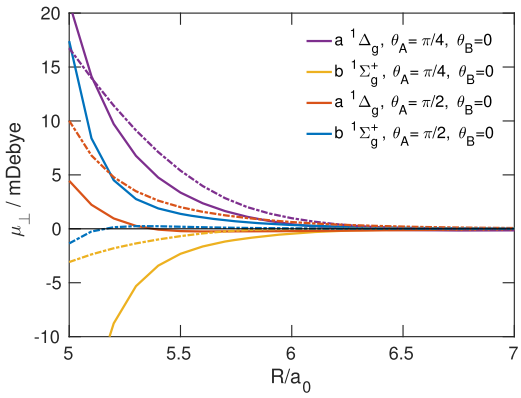

FIG. 6. The transition dipole perpendicular to the plane of coplanar system, $\phi = 0$, for selected θ_A and $\theta_B = 0$. Colors correspond to orientations and excited state asymptote, $O_2(X^3\Sigma_g^-) - O_2(a^1\Delta_g)$ or $O_2(X^3\Sigma_g^-) - O_2(b^1\Sigma_g^+)$. Solid lines correspond to calculations at the MRCI level, whereas the dashed-dotted lines were obtained at the CASSCF level of theory.

We note that both the magnitude and the shape of the transition dipole moment surface are strongly dependent on the level of theory at which they are calculated, and therefore it is impossible to make conclusive statements about the shape or magnitude of the true transition dipole surfaces. Nevertheless, at either level of theory, the transition dipole moment is a smooth albeit strongly anisotropic function of the nuclear geometry, which varies roughly exponentially with the intermolecular separation. The angular expansion is accurate to about 2.5% at $R = 6.5\ a_0$, which is the region most relevant for collision-induced absorption,[44] somewhat short of the classical turning point of the isotropic potential. The angular expansion coefficients, especially the more dominant terms, can be accurately represented using the reported exponentially extrapolating interpolation scheme. This is validated by extrapolating the obtained fit to short separations $R = 5.25\ a_0$. The fit reproduces the *ab initio* points to about 10% accuracy, even at this short separation which is both not included in the fit and to which the dynamics should be insensitive as the isotropic potential is highly repulsive.

VII. CONCLUSIONS

In the present paper, we have studied the four-dimensional diabatic potential energy surfaces and transition dipole moment surfaces of O_2–O_2, for the triplet states in which the monomers are in the $X^3\Sigma_g^-$, $a^1\Delta_g$, and $b^1\Sigma_g^+$ electronic states. These potentials and dipole moment surfaces are relevant for the atmospheric collision-induced absorption spectroscopy of the $X^3\Sigma_g^- \rightarrow a^1\Delta_g$ and $X^3\Sigma_g^- \rightarrow b^1\Sigma_g^+$ transitions, which are studied in Paper II.[10,44] At high-symmetry geometries, we have performed benchmark calculations of both the interaction energy and transition dipole moment. These indicate that the well depth of the potential may be reasonably well converged at the singles and doubles F12-MRCI+Q level, using an affordable active space containing only the O_2 π and π^* orbitals. The convergence of the interaction-induced transition dipole moment with the treatment of electron correlation is less smooth, which is rather surprising for a one-electron property, but in agreement with Ref. 23 which presented

the calculation of transition dipole moments of the double $a^1\Delta_g \rightarrow X^3\Sigma_g^-$ transition in O_2–O_2. We cannot conclude that any of our calculations of the dipole moment is converged, so we decided to compute full dipole moment surfaces at two levels of theory, such that the difference may be indicative of the uncertainty.

We computed adiabatic potentials at the F12-MRCI+Q level and dipole surfaces at the MRCI and CASSCF levels of theory and transformed these to the diabatic representation using the multiple-property-based diabatization algorithm in Ref. 9. We included the quadrupole tensor, electronic orbital angular momentum, and spin-orbit coupling in this multiple-property-based diabatization. The computed diabatic potentials and dipole surfaces were expanded in angular functions, with the expansion coefficients determined by numerical integration using Gauss-Legendre and Gauss-Chebyshev quadrature points. The radial dependence of these expansion coefficients was fit using an interpolation scheme that extrapolates exponentially to both short and large separations. For the exchange-interaction-induced properties studied here, this is more appropriate than the polynomial extrapolation of the popular RKHS interpolation scheme.[42] Also, we have provided a derivation of the restrictions that the high symmetry of the O_2–O_2 system imposes on the expansion coefficients of the diabatic potential energy and transition dipole surfaces. These symmetry constraints are fulfilled to numerical accuracy by the reported calculations. The diabatic potential energy surfaces and transition dipole moment surfaces are made available in the supplementary material.

The reported potential and dipole moment surfaces are used in subsequent dynamical calculations of the collision-induced absorption spectra.[10,44] However, such calculations cannot be fully predictive unless more accurate transition dipole moment surfaces can be determined. This remains an open question posed here as a challenge for developments in electronic structure theory.

SUPPLEMENTARY MATERIAL

See supplementary material for the diabatic potential energy surfaces and transition dipole moment surfaces.

ACKNOWLEDGMENTS

We thank the authors of Ref. 19 for sharing their global potential energy surfaces for the triplet ground state. We thank Xi Chu for sharing computational resources. T.K. acknowledges an STSM grant from European COST Action No. CM1405.

APPENDIX: SYMMETRY RESTRICTIONS ON THE ANGULAR EXPANSION

1. Potential energy surfaces

We first consider reflection in the xz-plane, which transforms the electronic Hamiltonian as

$$\sigma_{xz}\hat{\mathcal{H}}(\boldsymbol{r}_A,\boldsymbol{r}_B,\boldsymbol{R})\sigma_{xz}^\dagger = \hat{\mathcal{H}}(\sigma_{xz}\boldsymbol{r}_A,\sigma_{xz}\boldsymbol{r}_B,\sigma_{xz}\boldsymbol{R}). \tag{A1}$$

The action of this reflection on the electronic wavefunction is given by

$$\begin{aligned}\sigma_{xz}|\psi'_{A,\Lambda'_A}\psi'_{B,\Lambda'_B}\rangle^{(\boldsymbol{r}_A,\boldsymbol{r}_B,\boldsymbol{R})} &= \left[\sigma_{xz}\hat{\mathcal{T}}(\boldsymbol{R}/2)\hat{\mathcal{R}}(\boldsymbol{r}_A)|\psi_{A,\Lambda_A}(0,0,0)\rangle\right]\\ &\quad\otimes\left[\sigma_{xz}\hat{\mathcal{T}}(-\boldsymbol{R}/2)\hat{\mathcal{R}}(\boldsymbol{r}_B)|\psi_{B,\Lambda_B}(0,0,0)\rangle\right],\\ \sigma_{xz}\hat{\mathcal{T}}(\boldsymbol{R})\hat{\mathcal{R}}(\boldsymbol{r})|\psi_\Lambda(0,0,0)\rangle &= \sigma_{xz}\hat{\mathcal{T}}(\boldsymbol{R})\sigma_{xz}^\dagger\sigma_{xz}\\ &\quad\times\hat{\mathcal{R}}(\boldsymbol{r})\sigma_{xz}^\dagger\sigma_{xz}|\psi_\Lambda(0,0,0)\rangle.\end{aligned} \tag{A2}$$

The translation operator is transformed as

$$\begin{aligned}\sigma_{xz}\hat{\mathcal{T}}(\boldsymbol{R})\sigma_{xz}^\dagger &= \exp\left[-i\boldsymbol{R}\cdot\left(\sigma_{xz}\hat{\boldsymbol{P}}\sigma_{xz}^\dagger\right)\right]\\ &= \exp\left[-i\left(\sigma_{xz}\boldsymbol{R}\right)\cdot\hat{\boldsymbol{P}}\right] = \hat{\mathcal{T}}(\sigma_{xz}\boldsymbol{R}).\end{aligned} \tag{A3}$$

Noting that reflection of a vector replaces its azimuthal angle by its negative, we find for the rotation operator

$$\begin{aligned}\sigma_{xz}\hat{\mathcal{R}}(\boldsymbol{r})\sigma_{xz}^\dagger &= \sigma_{xz}\exp(-i\phi\hat{L}_z)\exp(-i\theta\hat{L}_y)\sigma_{xz}^\dagger\\ &= \exp(-i\phi\sigma_{xz}\hat{L}_z\sigma_{xz}^\dagger)\exp(-i\theta\hat{L}_y)\\ &= \exp(i\phi\hat{L}_z)\exp(-i\theta\hat{L}_y) = \hat{\mathcal{R}}(\sigma_{xz}\boldsymbol{r}).\end{aligned} \tag{A4}$$

For the action of $\hat{\sigma}_{xz}$ on the monomer functions, we use the following phase convention:

$$\begin{aligned}\hat{\sigma}_{xz}|X^3\Sigma_g^-\rangle &= (-1)^{\rho_{X^3\Sigma_g^-}}|X^3\Sigma_g^-\rangle = -|X^3\Sigma_g^-\rangle,\\ \hat{\sigma}_{xz}|a^1\Delta_{\pm2}\rangle &= (-1)^{\rho_{a^1\Delta_g}}|a^1\Delta_{\mp2}\rangle = |a^1\Delta_{\mp2}\rangle,\\ \hat{\sigma}_{xz}|b^1\Sigma_g^+\rangle &= (-1)^{\rho_{b^1\Sigma_g^+}}|b^1\Sigma_g^+\rangle = |b^1\Sigma_g^+\rangle,\end{aligned} \tag{A5}$$

i.e., the sign of the Λ quantum number is reversed, and a state-specific phase is obtained.

The above relations yield the identity

$$\begin{aligned}\langle\psi_{A,\Lambda_A}\psi_{B,\Lambda_B}|\hat{\mathcal{H}}|\psi'_{A,\Lambda'_A}\psi'_{B,\Lambda'_B}\rangle^{(\boldsymbol{r}_A,\boldsymbol{r}_B,\boldsymbol{R})} &= \langle\psi_{A,\Lambda_A}\psi_{B,\Lambda_B}|\sigma_{xz}^\dagger\sigma_{xz}\hat{\mathcal{H}}\sigma_{xz}^\dagger\sigma_{xz}|\psi'_{A,\Lambda'_A}\psi'_{B,\Lambda'_B}\rangle^{(\boldsymbol{r}_A,\boldsymbol{r}_B,\boldsymbol{R})}\\ &= (-1)^{\rho_{\psi_A}+\rho_{\psi_B}+\rho_{\psi'_A}+\rho_{\psi'_B}}\langle\psi_{A,-\Lambda_A}\psi_{B,-\Lambda_B}|\hat{\mathcal{H}}|\psi'_{A,-\Lambda'_A}\psi'_{B,-\Lambda'_B}\rangle^{(\sigma_{xz}\boldsymbol{r}_A,\sigma_{xz}\boldsymbol{r}_B,\sigma_{xz}\boldsymbol{R})}.\end{aligned} \tag{A6}$$

Next, we expand the matrix element in the first and the last steps above as in Eq. (21), and simplify the result using

$$\begin{aligned}D^{(l)*}_{m,k}(-\phi,\theta,0) &= (-1)^{k+m}D^{(l)*}_{-m,-k}(\phi,\theta,0),\\ \langle L_A,-M_A,L_B,-M_B|L-M\rangle &= (-1)^{L_A+L_B-L}\langle L_AM_AL_BM_B|LM\rangle,\end{aligned} \tag{A7}$$

and $(-1)^{\rho_{\psi_A}+\rho_{\psi_B}+\rho_{\psi'_A}+\rho_{\psi'_B}}=1$, assuming that the bra and ket correlate to the same asymptote. Equating like terms in both expansions, we find the following relation between the expansion coefficients:

$$\mathcal{V}^{\psi_{A,\Lambda_A},\psi_{B,\Lambda_B},\psi'_{A,\Lambda'_A},\psi'_{B,\Lambda'_B}}_{L_A,L_B,L}=(-1)^{L_A+L_B+L}\mathcal{V}^{\psi_{A,-\Lambda_A},\psi_{B,-\Lambda_B},\psi'_{A,-\Lambda'_A},\psi'_{B,-\Lambda'_B}}_{L_A,L_B,L}. \tag{A8}$$

Using the same approach as outlined above applied to the following identity, which results from the hermiticity of the electronic Hamiltonian,

$$\langle\psi_{A,\Lambda_A}\psi_{B,\Lambda_B}|\hat{\mathcal{H}}|\psi'_{A,\Lambda'_A}\psi'_{B,\Lambda'_B}\rangle^{(\boldsymbol{r}_A,\boldsymbol{r}_B,\boldsymbol{R})}=\left(\langle\psi'_{A,\Lambda'_A}\psi'_{B,\Lambda'_B}|\hat{\mathcal{H}}|\psi_{A,\Lambda_A}\psi_{B,\Lambda_B}\rangle^{(\boldsymbol{r}_A,\boldsymbol{r}_B,\boldsymbol{R})}\right)^*, \tag{A9}$$

we obtain

$$\mathcal{V}^{\psi_{A,\Lambda_A},\psi_{B,\Lambda_B},\psi'_{A,\Lambda'_A},\psi'_{B,\Lambda'_B}}_{L_A,L_B,L}=(-1)^{L_A+L_B+L}\left(\mathcal{V}^{\psi'_{A,\Lambda'_A},\psi'_{B,\Lambda'_B},\psi_{A,\Lambda_A},\psi_{B,\Lambda_B}}_{L_A,L_B,L}\right)^*. \tag{A10}$$

Further restrictions are derived from invariance under time reversal, $\hat{\mathcal{H}}=\hat{\theta}\hat{\mathcal{H}}\hat{\theta}^\dagger$, where $\hat{\theta}$ is the anti-unitary time-reversal operator. The action of time reversal on the spatial part of the electronic wavefunction is given by complex conjugation and within the adopted phase convention is identical to the action of $\hat{\sigma}_{xz}$, in Eq. (A6). Time reversal however also acts on the electronic spin coordinates as

$$\hat{\theta}|(S_AS_B)SM_S\rangle=(-1)^{S-M_S}|(S_AS_B)S,\ -M_S\rangle. \tag{A11}$$

Combining these relations, we obtain

$$\begin{aligned}\langle\psi_{A,\Lambda_A}\psi_{B,\Lambda_B}|\hat{\mathcal{H}}|\psi'_{A,\Lambda'_A}\psi'_{B,\Lambda'_B}\rangle^{(\boldsymbol{r}_A,\boldsymbol{r}_B,\boldsymbol{R})}&=\langle\psi_{A,\Lambda_A}\psi_{B,\Lambda_B}|\hat{\theta}^\dagger\hat{\theta}\hat{\mathcal{H}}\hat{\theta}^\dagger\hat{\theta}|\psi'_{A,\Lambda'_A}\psi'_{B,\Lambda'_B}\rangle^{(\boldsymbol{r}_A,\boldsymbol{r}_B,\boldsymbol{R})}\\&=(-1)^{\rho_{\psi_A}+\rho_{\psi_B}+\rho_{\psi'_A}+\rho_{\psi'_B}}\left(\langle\psi_{A,-\Lambda_A}\psi_{B,-\Lambda_B}|\hat{\mathcal{H}}|\psi'_{A,-\Lambda'_A}\psi'_{B,-\Lambda'_B}\rangle^{(\boldsymbol{r}_A,\boldsymbol{r}_B,\boldsymbol{R})}\right)^*,\end{aligned} \tag{A12}$$

where the spin-dependent phase equals unity as bra and ket correspond to the same total electron spin. Again assuming that the bra and ket correlate to the same asymptote, $(-1)^{\rho_{\psi_A}+\rho_{\psi_B}+\rho_{\psi'_A}+\rho_{\psi'_B}}=1$, we obtain the following relation between expansion coefficients:

$$\mathcal{V}^{\psi_{A,\Lambda_A},\psi_{B,\Lambda_B},\psi'_{A,\Lambda'_A},\psi'_{B,\Lambda'_B}}_{L_A,L_B,L}=(-1)^{L_A+L_B+L}\left(\mathcal{V}^{\psi_{A,-\Lambda_A},\psi_{B,-\Lambda_B},\psi'_{A,-\Lambda'_A},\psi'_{B,-\Lambda'_B}}_{L_A,L_B,L}\right)^*. \tag{A13}$$

The symmetries discussed above–rotational invariance, inversion symmetry, hermiticity of the Hamiltonian, and time-reversal symmetry–are always present. The O_2–O_2 system has even higher symmetry which is related to the permutation of identical nuclei. Therefore, we can also consider the permutation of nuclei within each monomer, $\mathcal{P}^{(A)}_{12}$ and $\mathcal{P}^{(B)}_{12}$, and the permutation of the monomers, $\mathcal{P}_{AB}$. From these symmetries, we obtain the relations

$$\begin{aligned}\hat{\mathcal{H}}(\boldsymbol{r}_A,\boldsymbol{r}_B,\boldsymbol{R})&=\hat{\mathcal{H}}(-\boldsymbol{r}_A,\boldsymbol{r}_B,\boldsymbol{R})\\&=\hat{\mathcal{H}}(\boldsymbol{r}_A,-\boldsymbol{r}_B,\boldsymbol{R})=\hat{\mathcal{H}}(\boldsymbol{r}_B,\boldsymbol{r}_A,-\boldsymbol{R}).\end{aligned} \tag{A14}$$

Using for the rotation operator

$$\begin{aligned}\hat{\mathcal{R}}(\boldsymbol{r})&=\hat{\mathcal{R}}_z(\phi)\hat{\mathcal{R}}_y(\theta)=\hat{\mathcal{R}}_z(\phi+\pi)\hat{\mathcal{R}}_y(\pi-\theta)\hat{\mathcal{R}}_y(\pi)\hat{\mathcal{R}}_z(\pi)\\&=\hat{\mathcal{R}}(-\boldsymbol{r})\hat{\imath}\sigma_{xz}(-1)^{\hat{L}_z},\end{aligned} \tag{A15}$$

where $\hat{\imath}$ inverts the electronic coordinates, we find for the *gerade* electronic wavefunctions

$$\begin{aligned}|\psi_{A,\Lambda_A}\psi_{B,\Lambda_B}\rangle^{(\boldsymbol{r}_A,\boldsymbol{r}_B,\boldsymbol{R})}&=(-1)^{\rho_{\psi_A}+\Lambda_A}|\psi_{A,-\Lambda_A}\psi_{B,\Lambda_B}\rangle^{(-\boldsymbol{r}_A,\boldsymbol{r}_B,\boldsymbol{R})}\\&=(-1)^{\rho_{\psi_B}+\Lambda_B}|\psi_{A,\Lambda_A}\psi_{B,-\Lambda_B}\rangle^{(\boldsymbol{r}_A,-\boldsymbol{r}_B,\boldsymbol{R})}.\end{aligned} \tag{A16}$$

Expanding each matrix element in

$$\begin{aligned}\langle\psi_{A,\Lambda_A}\psi_{B,\Lambda_B}|\hat{\mathcal{H}}|\psi'_{A,\Lambda'_A}\psi'_{B,\Lambda'_B}\rangle^{(\boldsymbol{r}_A,\boldsymbol{r}_B,\boldsymbol{R})}&=(-1)^{\rho_{\psi_A}+\Lambda_A+\rho_{\psi'_A}+\Lambda'_A}\langle\psi_{A,-\Lambda_A}\psi_{B,\Lambda_B}|\hat{\mathcal{H}}|\psi'_{A,-\Lambda'_A}\psi'_{B,\Lambda'_B}\rangle^{(-\boldsymbol{r}_A,\boldsymbol{r}_B,\boldsymbol{R})}\\&=(-1)^{\rho_{\psi_B}+\Lambda_B+\rho_{\psi'_B}+\Lambda'_B}\langle\psi_{A,\Lambda_A}\psi_{B,-\Lambda_B}|\hat{\mathcal{H}}|\psi'_{A,\Lambda'_A}\psi'_{B,-\Lambda'_B}\rangle^{(\boldsymbol{r}_A,-\boldsymbol{r}_B,\boldsymbol{R})},\end{aligned} \tag{A17}$$

we obtain the relations

$$\begin{aligned}\mathcal{V}^{\psi_{A,\Lambda_A},\psi_{B,\Lambda_B},\psi'_{A,\Lambda'_A},\psi'_{B,\Lambda'_B}}_{L_A,L_B,L}&=(-1)^{L_A+\rho_{\psi_A}+\rho_{\psi'_A}}\mathcal{V}^{\psi_{A,-\Lambda_A},\psi_{B,\Lambda_B},\psi'_{A,-\Lambda'_A},\psi'_{B,\Lambda'_B}}_{L_A,L_B,L},\\\mathcal{V}^{\psi_{A,\Lambda_A},\psi_{B,\Lambda_B},\psi'_{A,\Lambda'_A},\psi'_{B,\Lambda'_B}}_{L_A,L_B,L}&=(-1)^{L_B+\rho_{\psi_B}+\rho_{\psi'_B}}\mathcal{V}^{\psi_{A,\Lambda_A},\psi_{B,-\Lambda_B},\psi'_{A,\Lambda'_A},\psi'_{B,-\Lambda'_B}}_{L_A,L_B,L}.\end{aligned} \tag{A18}$$

Using the anti-symmetry of the electronic wavefunctions with respect to electron exchange, we obtain

$$|\psi_{A,\Lambda_A}\psi_{B,\Lambda_B}\rangle^{(\boldsymbol{r}_A,\boldsymbol{r}_B,\boldsymbol{R})} = (-1)^{n_e+S_A+S_B-S}|\psi_{B,\Lambda_B}\psi_{A,\Lambda_A}\rangle^{(\boldsymbol{r}_B,\boldsymbol{r}_A,-\boldsymbol{R})}, \tag{A19}$$

where n_e is the number of electrons of one O_2 moiety. Hence, by expanding both sides of

$$\langle\psi_{A,\Lambda_A}\psi_{B,\Lambda_B}|\hat{\mathcal{H}}|\psi'_{A,\Lambda'_A}\psi'_{B,\Lambda'_B}\rangle^{(\boldsymbol{r}_A,\boldsymbol{r}_B,\boldsymbol{R})} = (-1)^{S_A+S_B+S'_A+S'_B}\langle\psi_{B,\Lambda_B}\psi_{A,\Lambda_A}|\hat{\mathcal{H}}|\psi'_{B,\Lambda'_B}\psi'_{A,\Lambda'_A}\rangle^{(\boldsymbol{r}_B,\boldsymbol{r}_A,-\boldsymbol{R})}, \tag{A20}$$

we obtain the following symmetry:

$$\mathcal{V}^{\psi_{A,\Lambda_A},\psi_{B,\Lambda_B},\psi'_{A,\Lambda'_A},\psi'_{B,\Lambda'_B}}_{L_A,L_B,L} = (-1)^{L_A+L_B}\mathcal{V}^{\psi_{B,\Lambda_B},\psi_{A,\Lambda_A},\psi'_{B,\Lambda'_B},\psi'_{A,\Lambda'_A}}_{L_B,L_A,L}, \tag{A21}$$

where we have assumed $(-1)^{S_A+S_B+S'_A+S'_B} = 1$, which is always the case unless bra and ket correspond to states correlating to different asymptotes.

2. Dipole moment surfaces

We use the center of mass as the origin and an otherwise arbitrary space-fixed coordinate system. With this choice of origin, the nuclei do not contribute to the dipole moment, and the dipole operator is just the negative of the electronic position operator. Therefore, the action of a reflection in the xz-plane is given by

$$\sigma_{xz}\mu_\nu\sigma^\dagger_{xz} = \mu_{-\nu}. \tag{A22}$$

Expanding both sides of

$$\langle\psi_{A,\Lambda_A}\psi_{B,\Lambda_B}|\hat{\mu}_\nu|\psi'_{A,\Lambda'_A}\psi'_{B,\Lambda'_B}\rangle^{(\boldsymbol{r}_A,\boldsymbol{r}_B,\boldsymbol{R})} = (-1)^{\rho_{\psi_A}+\rho_{\psi_B}+\rho_{\psi'_A}+\rho_{\psi'_B}}\langle\psi_{A,-\Lambda_A}\psi_{B,-\Lambda_B}|\hat{\mu}_{-\nu}|\psi'_{A,-\Lambda'_A}\psi'_{B,-\Lambda'_B}\rangle^{(\sigma_{xz}\boldsymbol{r}_A,\sigma_{xz}\boldsymbol{r}_B,\sigma_{xz}\boldsymbol{R})}, \tag{A23}$$

we obtain the following relation:

$$\mathcal{D}^{\psi_{A,\Lambda_A},\psi_{B,\Lambda_B},\psi'_{A,\Lambda'_A},\psi'_{B,\Lambda'_B}}_{L_A,L_B,\lambda,L} = (-1)^{L_A+L_B+L}\mathcal{D}^{\psi_{A,-\Lambda_A},\psi_{B,-\Lambda_B},\psi'_{A,-\Lambda'_A},\psi'_{B,-\Lambda'_B}}_{L_A,L_B,\lambda,L}. \tag{A24}$$

In deriving the above, we assumed $(-1)^{\rho_{\psi_A}+\rho_{\psi_B}+\rho_{\psi'_A}+\rho_{\psi'_B}} = -1$, as is the case for the transition dipole moments coupling $|X^3\Sigma_g^-X^3\Sigma_g^-\rangle$ with states where one of the molecules is in the $X^3\Sigma_g^-$ state and the other is in the $a^1\Delta_g$ state or $b^1\Sigma_g^+$ state.

From symmetry under Hermitian conjugation

$$\hat{\mu}^\dagger_\nu = (-1)^\nu\hat{\mu}_{-\nu}, \tag{A25}$$

we obtain the relation

$$\mathcal{D}^{\psi_{A,\Lambda_A},\psi_{B,\Lambda_B},\psi'_{A,\Lambda'_A},\psi'_{B,\Lambda'_B}}_{L_A,L_B,\lambda,L} = (-1)^{L_A+L_B+L+1}\left(\mathcal{D}^{\psi'_{A,\Lambda'_A},\psi'_{B,\Lambda'_B},\psi_{A,\Lambda_A},\psi_{B,\Lambda_B}}_{L_A,L_B,\lambda,L}\right)^*. \tag{A26}$$

From time-reversal symmetry, we obtain

$$\mathcal{D}^{\psi_{A,\Lambda_A},\psi_{B,\Lambda_B},\psi'_{A,\Lambda'_A},\psi'_{B,\Lambda'_B}}_{L_A,L_B,\lambda,L} = (-1)^{L_A+L_B+L+1}\left(\mathcal{D}^{\psi_{A,-\Lambda_A},\psi_{B,-\Lambda_B},\psi'_{A,-\Lambda'_A},\psi'_{B,-\Lambda'_B}}_{L_A,L_B,\lambda,L}\right)^*. \tag{A27}$$

Next, we obtain relations between the expansion coefficients which are valid only if permutation symmetry of identical nuclei is present. Expanding each matrix element in the relations obtained from $\mathcal{P}^{(A)}_{12}$ and $\mathcal{P}^{(B)}_{12}$,

$$\begin{aligned}\langle\psi_{A,\Lambda_A}\psi_{B,\Lambda_B}|\hat{\mu}_\nu|\psi'_{A,\Lambda'_A}\psi'_{B,\Lambda'_B}\rangle^{(\boldsymbol{r}_A,\boldsymbol{r}_B,\boldsymbol{R})} &= (-1)^{\rho_{\psi_A}+\Lambda_A+\rho_{\psi'_A}+\Lambda'_A}\langle\psi_{A,-\Lambda_A}\psi_{B,\Lambda_B}|\hat{\mu}_\nu|\psi'_{A,-\Lambda'_A}\psi'_{B,\Lambda'_B}\rangle^{(-\boldsymbol{r}_A,\boldsymbol{r}_B,\boldsymbol{R})}\\ &= (-1)^{\rho_{\psi_B}+\Lambda_B+\rho_{\psi'_B}+\Lambda'_B}\langle\psi_{A,\Lambda_A}\psi_{B,-\Lambda_B}|\hat{\mu}_\nu|\psi'_{A,\Lambda'_A}\psi'_{B,-\Lambda'_B}\rangle^{(\boldsymbol{r}_A,-\boldsymbol{r}_B,\boldsymbol{R})},\end{aligned} \tag{A28}$$

we obtain the relations

$$\begin{aligned}\mathcal{D}^{\psi_{A,\Lambda_A},\psi_{B,\Lambda_B},\psi'_{A,\Lambda'_A},\psi'_{B,\Lambda'_B}}_{L_A,L_B,\lambda,L} &= (-1)^{L_A+\rho_{\psi_A}+\rho_{\psi'_A}}\mathcal{D}^{\psi_{A,-\Lambda_A},\psi_{B,\Lambda_B},\psi'_{A,-\Lambda'_A},\psi'_{B,\Lambda'_B}}_{L_A,L_B,\lambda,L},\\ \mathcal{D}^{\psi_{A,\Lambda_A},\psi_{B,\Lambda_B},\psi'_{A,\Lambda'_A},\psi'_{B,\Lambda'_B}}_{L_A,L_B,\lambda,L} &= (-1)^{L_B+\rho_{\psi_B}+\rho_{\psi'_B}}\mathcal{D}^{\psi_{A,\Lambda_A},\psi_{B,-\Lambda_B},\psi'_{A,\Lambda'_A},\psi'_{B,-\Lambda'_B}}_{L_A,L_B,\lambda,L}.\end{aligned} \tag{A29}$$

Similarly, we obtain from $\mathcal{P}_{AB}$ the relation

$$\langle\psi_{A,\Lambda_A}\psi_{B,\Lambda_B}|\hat{\mu}_\nu|\psi'_{A,\Lambda'_A}\psi'_{B,\Lambda'_B}\rangle^{(\boldsymbol{r}_A,\boldsymbol{r}_B,\boldsymbol{R})} = (-1)^{S_A+S_B+S'_A+S'_B}\langle\psi_{B,\Lambda_B}\psi_{A,\Lambda_A}|\hat{\mu}_\nu|\psi'_{B,\Lambda'_B}\psi'_{A,\Lambda'_A}\rangle^{(\boldsymbol{r}_B,\boldsymbol{r}_A,-\boldsymbol{R})}, \tag{A30}$$

from which we obtain the following symmetry:

$$\mathcal{D}^{\psi_{A,\Lambda_A},\psi_{B,\Lambda_B},\psi'_{A,\Lambda'_A},\psi'_{B,\Lambda'_B}}_{L_A,L_B,\lambda,L} = (-1)^{L_A+L_B+\lambda+L+1}\mathcal{D}^{\psi_{B,\Lambda_B},\psi_{A,\Lambda_A},\psi'_{B,\Lambda'_B},\psi'_{A,\Lambda'_A}}_{L_B,L_A,\lambda,L}. \tag{A31}$$

Here, we have assumed $(-1)^{S_A+S_B+S'_A+S'_B} = -1$, which is always valid for the transition moments connecting $|X^3\Sigma_g^-X^3\Sigma_g^-\rangle$ with any of the other states.

[1]T. G. Slanger and R. A. Copeland, Chem. Rev. **103**, 4731 (2003).
[2]C. Frankenberg, R. Pollock, R. A. M. Lee, J. Rosenberg-Blavier, D. Crisp, C. W. O'Dell, G. B. Osterman, C. Roehl, P. O. Wennberg, and D. Wunch, Atmos. Meas. Techniques. Discuss. **7**, 7641 (2014).
[3]B. Buijsse, W. J. van der Zande, A. T. J. B. Eppink, D. H. Parker, B. R. Lewis, and S. T. Gibson, J. Chem. Phys. **108**, 7229 (1998).
[4]B. Minaev, O. Vahtras, and H. Ågren, Chem. Phys. **208**, 299 (1996).
[5]D. L. A. G. Grimminck, F. R. Spiering, L. M. C. Janssen, A. van der Avoird, W. J. van der Zande, and G. C. Groenenboom, J. Chem. Phys. **140**, 204314 (2014).
[6]I. E. Gordon, S. Kassi, A. Campargue, and G. C. Toon, J. Quant. Spectrosc. Radiat. Transfer **111**, 1174 (2010).
[7]B. Minaev, J. Mol. Struct.: THEOCHEM **183**, 207 (1989).
[8]D. A. Long and J. T. Hodges, J. Geophys. Res.: Atmos. **117**, D12309, doi: 10.1029/2012JD017807 (2012).
[9]T. Karman, A. van der Avoird, and G. C. Groenenboom, J. Chem. Phys. **144**, 121101 (2016).
[10]T. Karman, M. A. J. Koenis, A. Banerjee, D. H. Parker, I. E. Gordon, A. van der Avoird, W. J. van der Zande, and G. C. Groenenboom, "Mechanisms of collision-induced absorption for spin-forbidden transitions" (unpublished).
[11]M. C. van Hemert, P. E. S. Wormer, and A. van der Avoird, Phys. Rev. Lett. **51**, 1167 (1983).
[12]P. E. S. Wormer and A. van der Avoird, J. Chem. Phys. **81**, 1929 (1984).
[13]B. Bussery and P. E. S. Wormer, J. Chem. Phys. **99**, 1230 (1993).
[14]V. Aquilanti, D. Ascenzi, M. Bartolomei, D. Cappelletti, S. Cavalli, M. de Castro Vìtores, and F. Pirani, Phys. Rev. Lett. **82**, 69 (1999).
[15]V. Aquilanti, D. Ascenzi, M. Bartolomei, D. Cappelletti, S. Cavalli, M. de Castro Vìtores, and F. Pirani, J. Am. Chem. Soc. **121**, 10794 (1999).
[16]R. Hernández-Lamoneda, M. Bartolomei, M. I. Hernández, J. Campos-Martínez, and F. Dayou, J. Phys. Chem. A **109**, 11587 (2005).
[17]M. Bartolomei, E. Carmona-Novillo, M. I. Hernández, J. Campos-Martínez, and R. Hernández-Lamoneda, J. Chem. Phys. **128**, 214304 (2008).
[18]M. Bartolomei, M. I. Hernández, J. Campos-Martínez, E. Carmona-Novillo, and R. Hernández-Lamoneda, Phys. Chem. Chem. Phys. **10**, 5374 (2008).
[19]M. Bartolomei, E. Carmona-Novillo, M. I. Hernández, J. Campos-Martínez, and R. Hernández-Lamoneda, J. Chem. Phys. **133**, 124311 (2010).
[20]J. Liu and K. Morokuma, J. Chem. Phys. **123**, 204319 (2005).
[21]F. Dayou, M. I. Hernández, J. Campos-Martínez, and R. Hernández-Lamoneda, J. Chem. Phys. **123**, 074311 (2005).
[22]F. Dayou, M. I. Hernández, J. Campos-Martínez, and R. Hernández-Lamoneda, J. Chem. Phys. **126**, 194309 (2007).
[23]M. V. Zagidullin, A. A. Pershin, V. N. Azyazov, and A. M. Mebel, J. Chem. Phys. **143**, 244315 (2015).
[24]B. F. Minaev, J. Appl. Spectrosc. **42**, 518 (1985).
[25]B. F. Minaev, Russ. Chem. Rev. **76**, 1059 (2007).
[26]P. E. S. Wormer, J. A. Kłos, G. C. Groenenboom, and A. van der Avoird, J. Chem. Phys. **122**, 244325 (2005).
[27]R. P. Leavitt, J. Chem. Phys. **72**, 3472 (1980).
[28]G. C. Groenenboom, X. Chu, and R. V. Krems, J. Chem. Phys. **126**, 204306 (2007).
[29]A. van der Avoird, P. E. S. Wormer, F. Mulder, and R. M. Berns, Top. Curr. Chem. **93**, 1 (1980).
[30]H. B. G. Casimir and D. Polder, Phys. Rev. **73**, 360 (1948).
[31]J. E. Bohr and K. L. C. Hunt, J. Chem. Phys. **86**, 5441 (1987).
[32]J. H. van Lenthe and F. B. van Duijneveldt, J. Chem. Phys. **81**, 3168 (1984).
[33]T. Shiozaki, G. Knizia, and H.-J. Werner, J. Chem. Phys. **134**, 034113 (2011).
[34]T. Shiozaki and H.-J. Werner, J. Chem. Phys. **133**, 141103 (2010).
[35]T. H. Dunning, J. Chem. Phys. **90**, 1007 (1989).
[36]F. Weigend, A. Köhn, and C. Hättig, J. Chem. Phys. **116**, 3175 (2002).
[37]F. Weigend, Phys. Chem. Chem. Phys. **4**, 4285 (2002).
[38]H.-J. Werner, P. J. Knowles *et al.*, MOLPRO, version 2012.1, a package of *ab initio* programs, 2012, see http://www.molpro.net.
[39]S. F. Boys and F. Bernardi, Mol. Phys. **19**, 553 (1970).
[40]M. C. G. N. van Vroonhoven and G. C. Groenenboom, J. Chem. Phys. **116**, 1954 (2002).
[41]T. Karman, X. Chu, and G. C. Groenenboom, Phys. Rev. A **90**, 052701 (2014).
[42]T.-S. Ho and H. Rabitz, J. Chem. Phys. **104**, 2584 (1996).
[43]M. Bartolomei, E. Carmona-Novillo, M. I. Hernández, J. Campos-Martínez, and R. Hernández-Lamoneda, J. Comput. Chem. **32**, 279 (2011).
[44]T. Karman, A. van der Avoird, and G. C. Groenenboom, J. Chem. Phys. **147**, 084307 (2017).